Naval Research Laboratory

Washington, DC 20375-5320

NRL/MR/7130--15-9623

Structural Acoustic UXO Detection and Identification in Marine Environments — Interim Report for SERDP MR-2103 Follow-On

J.A. Bucaro

Excet, Inc.
Springfield, Virginia

A. Sarkissian
B.H. Houston
M. Saniga
H. Simpson
Z.J. Waters
D. Amon
E. Williams
N. Valdivia
T. Yoder

Physical Acoustics Branch
Acoustics Division

K. Jig
S. Liskey

Sotera Defense Technology & Systems, Inc.
Columbia, Maryland

July 30, 2015

Approved for public release; distribution is unlimited.

REPORT DOCUMENTATION PAGE

Form Approved
OMB No. 0704-0188

Public reporting burden for this collection of information is estimated to average 1 hour per response, including the time for reviewing instructions, searching existing data sources, gathering and maintaining the data needed, and completing and reviewing this collection of information. Send comments regarding this burden estimate or any other aspect of this collection of information, including suggestions for reducing this burden to Department of Defense, Washington Headquarters Services, Directorate for Information Operations and Reports (0704-0188), 1215 Jefferson Davis Highway, Suite 1204, Arlington, VA 22202-4302. Respondents should be aware that notwithstanding any other provision of law, no person shall be subject to any penalty for failing to comply with a collection of information if it does not display a currently valid OMB control number. **PLEASE DO NOT RETURN YOUR FORM TO THE ABOVE ADDRESS.**

1. REPORT DATE *(DD-MM-YYYY)*
30-07-2015

2. REPORT TYPE
NRL Memorandum Report

3. DATES COVERED *(From - To)*
01 December 2014 – 31 December 2015

4. TITLE AND SUBTITLE
Structural Acoustic UXO Detection and Identification in Marine Environments — Interim Report for SERDP MR-2103 Follow-On

5a. CONTRACT NUMBER

5b. GRANT NUMBER

5c. PROGRAM ELEMENT NUMBER

5d. PROJECT NUMBER MR-2103

5e. TASK NUMBER

5f. WORK UNIT NUMBER

6. AUTHOR(S)
J.A. Bucaro,[1] A. Sarkissian, B.H. Houston, M. Saniga, H. Simpson, Z.J. Waters, D. Amon, E. Williams, N. Valdivia, T. Yoder, K. Jig,[2] and S. Liskey[2]

7. PERFORMING ORGANIZATION NAME(S) AND ADDRESS(ES)
Naval Research Laboratory, Code 6390
4555 Overlook Avenue, SW
Washington, DC 20375-5320

8. PERFORMING ORGANIZATION REPORT NUMBER
NRL/MR/7130--15-9623

9. SPONSORING / MONITORING AGENCY NAME(S) AND ADDRESS(ES)
SERDP Program Office
901 North Stuart Street, Suite 303
Arlington, VA 22203

10. SPONSOR / MONITOR'S ACRONYM(S)
SERDP

11. SPONSOR / MONITOR'S REPORT NUMBER(S)

12. DISTRIBUTION / AVAILABILITY STATEMENT
Approved for public release; distribution is unlimited.

13. SUPPLEMENTARY NOTES
[1]Excet, Inc., 8001 Braddock Road, Suite 303, Springfield, VA 22151
[2]Sotera Defense Technology & Systems, Inc., 7230 Lee DeForest Drive, Suite 100, Columbia, MD 21046-2350

14. ABSTRACT
SERDP goals require the development of sonar technologies able to separate UXO and false target detections. The specific goal addressed in the work reported here is to complete analysis studies using the data collected in June 2013 in the Gulf of Mexico using the BOSS-40 sonar. The measurements and post measurement analysis (PMA) results have been described in the April 2014 MR2103 Final Report.

15. SUBJECT TERMS
Underwater Buried UXO
Sonar UXO detection
Structural acoustic target identification

16. SECURITY CLASSIFICATION OF:			17. LIMITATION OF ABSTRACT	18. NUMBER OF PAGES	19a. NAME OF RESPONSIBLE PERSON
a. REPORT	b. ABSTRACT	c. THIS PAGE			B.H. Houston
Unclassified Unlimited	Unclassified Unlimited	Unclassified Unlimited	Unclassified Unlimited	35	19b. TELEPHONE NUMBER *(include area code)* (202) 404-3840

Standard Form 298 (Rev. 8-98)
Prescribed by ANSI Std. Z39.18

TABLE OF CONTENTS

LIST OF TABLES iv

LIST OF FIGURES iv

LIST OF ACRONYMS vi

ACKNOWLEDGEMENTS vi

ABSTRACT 1

OBJECTIVE 2

TECHNICAL APPROACH 2

RESULTS AND DISCUSSION 4

SUBTASK 2.4. Re-configure imaging algorithm and include AUV position data and north/south AUV path data 4

SUBTASK 2.5. Include North/South AUV multiple path data in target separation study.... 14

SUBTASK 2.6. Include all additional proud targets (+16) in the RVM target separation study 17

SUBTASK 2.7. Analyze acoustic color from non-epoxy-filled UXO (proud) compared to epoxy-filled (buried) UXO. 18

SUBTASK 2.8. Perform acoustic BOSS source calibration in the NRL near-field holography facility. 20

Subtask 2.9 Using new BOSS source calibration data, generate and analyze specular-filtered plan view images of the buried UXO. 21

CONCLUSIONS TO DATE 23

LITERATURE CITED 24

APPENDIX 27

LIST OF TABLES

TABLE 1 – Proud and Buried Target List

LIST OF FIGURES

Figure 1. Drawing illustrating a BOSS flight path along x, the ping sequence, and the interrogated swath on the bottom.

Figure 2. Cartoon illustrating the Δz ambiguity for a sloping sediment when the flight paths are laterally far from the target.

Figure 3. The EW and NS flight paths executed by BOSS over the target field.

Figure 4a. The plan view and two depth images for N1 through N4 targets using EW flight path h.

Figure 4b. Plan view and two depth images for N5 through N8 targets using EW flight path h.

Figure 4c. Plan view and depth images for N9 - N11 targets using EW flight paths g,h, and c, respectively.

Figure 5a. The plan view and two depth images for N1 through N4 targets using NS flight paths e and k.

Figure 5b. The plan view and two depth images for N5 through N8 targets using NS flight paths m, o, and s.

Figure 5c. The plan view and two depth images for N9 through N11 targets using NS flight paths y, Ba, and v.

Figure 6. Assumed rock orientation with respect to x, y scans with its long axis rotated up out of the horizontal plane ~ 80° about the x axis.

Figure 7. The three 2-D images of the rock (N10) produced from the EW flight path h and from the NS flight path Ba.

Figure 8a. Discriminatively-trained RVM classification algorithm trained on even numbered source pings and tested on odd numbered pings. Targets include 9 buried UXO and 9 non-UXO – 2 buried and 7 proud. NS paths (3-20 kHz).

Figure 8b. Discriminatively-trained RVM classification algorithm trained on even numbered source pings and tested on odd numbered pings. Targets include 9 buried UXO and 9 non-UXO – 2 buried and 7 proud. NS paths (3-13.3 kHz).

Figure 9. Discriminatively-trained RVM classification algorithm trained on even numbered source pings and tested on odd numbered pings. Targets include 9 buried UXO and 8 non-UXO – 2 buried and 6 proud. EW paths (3 – 13.3 kHz).

Figure 10. ROC curves associated with the results in Fig 9.

Figure 11. Discriminatively-trained RVM classification algorithm trained on even numbered source pings and tested on odd numbered pings. Targets include 9 buried UXO and 9 non-UXO – 2 buried and 7 proud. NS paths (3-13.3 kHz).

Figure 12. ROC curve associated with the results in Fig 11.

Figure 13. Discriminatively-trained RVM classification algorithm trained/tested on even/odd numbered source pings, respectively. Targets: 9 buried and 10 proud UXO and 14 non-UXO – 2 buried and 12 proud. NS paths (3-13.3 kHz).

Figure 14a. RVM discriminative algorithm trained and tested on even and odd numbered source pings, respectively using the acoustic color maps. On average, we used epoxy-filled 155mm shell data from 7 EW paths and empty 155mm shell data from 5 EW paths.

Figure 14b. RVM discriminative algorithm trained and tested on even and odd numbered source pings, respectively using the acoustic color maps. On average, we used epoxy-filled 155mm shell data from 4 EW paths and empty 155mm shell data collected on 5 EW paths.

Figure 15. The NRL Structural Acoustic Pool facility.

Figure 16. The two orientations for hanging BOSS in the NRL Structural Acoustic Pool facility.

Figure 17. Source pressure levels in dB measured at the 5 receivers 3.4 meters from BOSS as it is rotated in steps of 0.5 degrees and what the pattern would be were the BOSS source omnidirectional.

Figure 18. The measured time waveforms at the 5 receivers.

Figure 19. The measured signal spectra measured at the 5 receivers.

Figure 20. Geometry describing the mapping between the measured source radiation pattern and the radiating source strength spatial distribution.

Figure 21. The supersonic images mapped onto the BOSS AUV upper half and the BOSS AUV lower half with a photo indicating the actual locations on BOSS.

Figure A1. Photograph of BOSS in the water.

Figure A2. Plan view and head-on view of BOSS.

Figure A3. Photograph of BOSS prior to complete assembly showing some of the internal components.

Figure A4. Preliminary 3-D images obtained from June 23, 2014 BOSS data by Richard Holtzapple and Nick Pineda.

LIST OF ACRONYMS

AUV	Autonomous Underwater Vehicle
BOSS	Buried Object Scanning Sonar
DVL	Doppler Velocity Log
EW	East/West
INU	Inertial Navigation Unit
NRL	Naval Research Laboratory
NSWC-PCD	Naval Surface Warfare Center – Panama City Division
NS	North/South
PMA	Post Measurement Analysis
RVM	Relevance Vector Machine
ROC	Receiver Operating Characteristic
SA	Structural Acoustic
SAS	Synthetic Aperture Sonar
S/N (SNR)	Signal to Noise
TREX	Transmission and Radiation Experiments
TS	Target Strength
TVR	Transducer Voltage Response
UXO	Unexploded Ordnance

ACKNOWLEDGEMENTS

This work was performed under direct support from the SERDP Program Office. We would like to acknowledge the very positive and encouraging program management role played by Dr. Herb Nelson, SERDP Program Manager for Munitions Response. We would also like to acknowledge the significant impact made in these studies by the leveraging of results from scientifically related efforts funded by ONR.

ABSTRACT

SERDP goals require the development of sonar technologies able to separate UXO and false target detections. The specific goal addressed in the work reported here is to complete analysis studies using the data collected in June 2013 in the Gulf of Mexico using the BOSS-40 sonar. The measurements and post measurement analysis (PMA) results have been described in the April 2014 MR2103 Final Report.

In the following, we describe the results of this PMA. In summary, inclusion of the AUV position data in the imaging algorithm has improved the quality of the images and their ability to correctly register buried targets with respect to the location of the sediment interface. We find that the performance of the RVM feature separation algorithm is slightly better for the NS paths than for the EW paths. Further, in a study that included all targets, the results demonstrate that the multi-dimensional feature extracted from acoustic color can separate the detections from the UXO/non-UXO groups and that this feature can be used to separate the epoxy-filled shells from the others. BOSS source calibration studies were completed demonstrating that the coupled source/AUV system does not radiate as a spherically radiating source and at any particular frequency, the acoustic pressure fluctuates considerably with direction. We find that the important structural acoustic interaction to consider is that between the spherical source, its mounting structure, and the associated short cylindrical section of the AUV. The next step is to integrate this information into our PMA of current and future BOSS data.

[1]

Manuscript approved March 25, 2015

OBJECTIVE

Many active and former military installations have ordnance ranges/training areas with adjacent water environments in which unexploded ordnance (UXO) now exists due to wartime activities, dumping, and accidents. SERDP goals require the development of innovative technologies[1-8] able to separate UXO from false targets and to discriminate amongst UXO targets themselves. The objective of the overall program is to address the scientific and technical issues whose resolution would result in an efficient, high performance structural acoustic (SA) feature-based underwater sonar technology that can detect and localize buried (and proud) targets and separate the detections into UXO vs non-UXO. Our focus is on marine-based sonars that could look both downward (and sideways) in water depths ranging from several meters to tens of meters. The overall goal here is to develop a sonar approach which results in robust identification algorithms based on structural acoustic features and complementary 3-D SAS (synthetic aperture sonar) images and to demonstrate the ability to detect and classify proud and buried UXO in the presence of natural and man-made clutter with actual structural acoustic sonar systems at-sea. The specific goal addressed in the work reported here is to complete additional analysis studies using the data collected in June 2013 in the Gulf of Mexico using the BOSS-40 sonar[9]. The measurements and previously obtained post measurement analysis (PMA) results have been described in Final Report "Structural Acoustic UXO Detection and Identification in Marine Environments, April 2014."[10]

TECHNICAL APPROACH

In June of 2013 NSWC, together with NRL and Bluefin Robotics, successfully flew the BOSS[9] structural acoustic sonar in the Gulf of Mexico over a target field in which were buried nine NRL epoxy-filled UXO's and 2 false targets and some 20 proud targets. Through this study we established (1) the ability to produce both 3-D images and target strength spatial/spectral maps of the buried targets and (2) that UXO targets and false targets can be separated using a multi-dimensional but otherwise straightforward feature set. The details of the BOSS system are described in the Appendix.

The general location of the target field was roughly 2 miles off the coast of Panama City, Florida. This location was the sight of a broader set of measurements made about the same time as part of the so-called TREX-13 exercise. For that program, a proud target field was created (see the proud targets listed in Table 1), and scattering measurements were carried out using sources and receivers mounted on towers along the northern perimeter of the target field. These assets were removed just prior to our exercise using the BOSS AUV system.

Table 1 - Proud and Buried Target List

Proud Targets				NRL Simulant–Filled Buried Targets	
T1	DEU Trainer	T14	Scuba Tank w/water w stem	N1	5inch Rocket nose-up 60°
T2	Rock	T15	2:1 Aspect Phone Pole Section	N2	5inch Rocket nose-up 30°
T3	55 Gallon Filled Drum	T17	2 ft Aluminum Cylinder	N3	5inch Rocket horizontal
T5	5:1 Aspect Phone Pole Section	T18	Cement Block	N4	155mm Projectile horizontal
T7	3ft Aluminum Cylinder	T19	Tire	N5	155mm Projectile horizontal 90°
T8	155mm Projectile w/o collar	T20	Aluminum UXO Replica	N6	155mm Projectile horizontal 20cm
T9	155mm Projectile w/ collar	T22	Original Material UXO	N7	155mm Projectile nose-up 30°
T10	Panel Target	T25	Bullet #1	N8	155mm Projectile nose-up 60°
T11	152 mm TP-T	T28	155mm Projectile w/collar	N9	120mm Mortar horizontal
T12	81mm Mortar	T29	Bullet #2	N10	Large Rock (no simulant)
T13	Scuba Tank w/water w/o stem	T30	Finned Shell #1	N11	Cinder Block (no simulant)

The nine buried NRL epoxy filled UXOs include three 5 inch rockets, five 155mm projectiles, and a 120mm mortar. The two buried NRL false targets included a large rock and a conventional cinder block. These eleven NRL targets were buried by Dr. Kevin Williams (Applied Physics Laboratory at University of Washington) and his diving team aided by Dr. Michael Richardson about three weeks before the BOSS exercise. The plan was to bury all but one of the NRL targets in such a way that the highest point of the target would be 10cm below the sediment-water interface. The one exception was to be a horizontally buried 155mm projectile at a 50cm depth. Generally, the divers executed the plan fairly well given the difficulty of burying such relatively large objects in 60 foot waters. Although it was not possible to know the burial condition of each target precisely, the general consensus was that the depth and orientation achieved for each target were roughly according to plan. Two exceptions were that the cinder block burial depth was less than 10cm and the deeply buried 155mm projectile was closer to 20cm from the sediment interface. There were 23 targets placed proud on the sediment. These included some UXOs not filled with epoxy, a rock, and a number of man-made objects. Together with the buried rock and cinderblock, 7 of these 23 proud targets serve as false targets in the target feature separation studies to be discussed later. These seven include the rock (T2), the 55 gallon water filled drum (T3), the 5:1 aspect telephone pole section (T5), the panel (T10 or CP), the 2:1 aspect telephone pole section (T15), the cement block (T18), and the tire (T19). The proud and buried targets in the target field are listed and labelled in Table 1. Their rough relative positions within the target field are illustrated in Fig. 44.

In this SERDP program (MR2103), we demonstrated the structural acoustic technology with an autonomous underwater vehicle (AUV) - based SA sonar successfully detecting UXO buried in the sediment in the Gulf of Mexico and showing that their structural acoustic features could be used to separate them from proud and buried false targets[10]. In particular, the Buried Object Scanning Sonar (BOSS)[9] was set up to fly at several meters altitudes in 60 foot water depths off the Coast of Panama, City in the Gulf of Mexico. This AUV-based sonar carried out north-south, east-west, and diagonal paths over a target field comprised of nine epoxy-filled UXOs buried about 10cm below the sediment/water interface, two buried false targets, and 23 proud targets. The scattered acoustic pressure signals from the target field received at each of the 40 wing sensors as the vehicle moved in a straight line were processed in a synthetic aperture manner yielding both 3-D images and several acoustic color constructs for all the buried targets and for seven of the proud targets considered to be non-UXO. Most of the images gave useful information related to

the target size and burial orientation. A multi-dimensional feature extracted from the acoustic color maps demonstrated almost perfect separation between the nine UXO and the nine false targets. These results demonstrate that typical buried UXO can be detected, imaged, and classified (UXO versus non-UXO) using a structural acoustic sonar and a relevance vector machine identification algorithm (RVM)[11]. In addition, earlier measurements made with a rail-based structural acoustic sonar in 25 foot waters off the Duck, NC coast validated the new concept of short time (specular) versus long time (elastic highlight)[12] plan view imaging. For reasons associated with the BOSS projector, such images could not be produced from the Gulf BOSS data. Finally, the first accomplishment early in the program involved the sediment pool demonstration of a numerically trained classifier. Here we demonstrated good classifier performance training the relevance vector machine algorithm on a finite element[13,14] target burial angle simulation data set and testing on UXO and false targets buried in the sediment pool[15].

In the work reported here, we carried out additional post measurement analysis on the data obtained using BOSS in the Gulf of Mexico[10]. Specifically, we prosecuted the following PMA tasks (numbered to be consistent with the subtasks reported in the previous report). Subtask 2.4: Re-configure imaging algorithm and include AUV position data and north/south AUV path data; Subtask 2.5: Include north/south AUV multiple path data in target separation study; Subtask 2.6: Include all additional proud targets (+16) in the RVM target separation study; Subtask 2.7: Analyze acoustic color from non-epoxy filled UXO (proud) compared to epoxy-filled (buried) UXO; Subtask 2.8: Perform acoustic BOSS source calibration in the NRL nearfield holography facility; and Subtask 2.9: Using new BOSS source calibration data, generate and analyze specular-filtered plan view images of the buried UXO.

RESULTS AND DISCUSSION

SUBTASK 2.4. Re-configure imaging algorithm and include AUV position data and north/south AUV path data

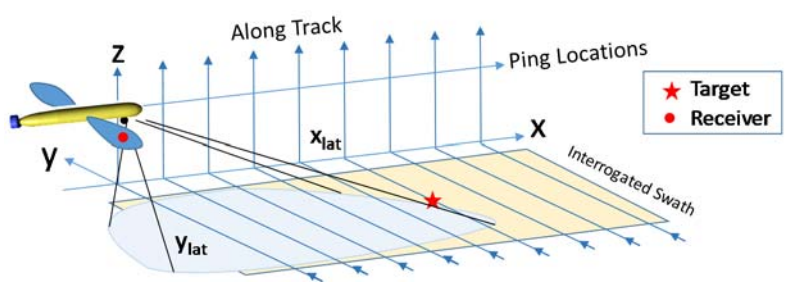

Figure 1. Drawing illustrating a BOSS flight path along x, the ping sequence, and the interrogated swath on the bottom.

The 3-D images[16,17] previously generated and reported in the Final Report[8] for MR2103 were generated in the following way. (See Fig. 1.) For the EW flight paths, the vehicle moved in the x or –x direction. To produce images or do SAS processing, the measured signal was initially time windowed to remove the bottom bounce (and everything arriving prior to it) and the surface reflection (with everything arriving after it). Next, using the measured acoustic signal from 40 pings (40 x positions of the vehicle), the image was produced as a function of x,y,z using data over the frequency range of 3 to 20 kHz. Next the images at the same (x,y,z) locations were produced from a different set of 40 pings starting from the 6th ping in the previous set. This was repeated to

produce a total of 33 image points at a given (x,y,z) location, each from a different set of 40 pings. Out of the 33 image points at a given (x,y,z) location, the maximum image value was chosen which became the final image point at that (x,y,z) location.

The images were obtained using the following time-delay beam-forming algorithm operating on the signals at the nth receiver to obtain the image strength at r_i.

$$\text{Image Strength at } \vec{r}_i \equiv \sigma_i\left(\vec{r}_i\right) = \frac{1}{N}\sum_{n=1}^{N} 4\pi\left|\vec{r}_n - \vec{r}_i\right| d_n\left(\vec{r}_n \middle| \vec{r}_i, \frac{\left|\vec{r}_n - \vec{r}_i\right|}{c}\right).$$

where d_n = Inverse Fourier transform of D_n and $D_n\left(\vec{r}_n \middle| \vec{r}_i, \omega\right) = \dfrac{P_n\left(\vec{r}_n \middle| \vec{r}_i, \omega\right)}{V(\omega)} = \sigma_i\left(\vec{r}_{,i}\omega\right)\dfrac{e^{ik\left|\vec{r}_n - \vec{r}_i\right|}}{4\pi\left|\vec{r}_n - \vec{r}_i\right|}$

Since we are interested in forming images over volumes about the size of a target, we can ignore the variation in the range dependent pre-factor in the image strength expression above.

To obtain a 2-d plot as a function of x and y (plan view image), the maximum image value as a function of z is chosen for a given (x,y) coordinate. Similarly, to obtain a plot as a function of y and z (a depth image), the maximum value along x is picked and the same with the plot as a function of x and z (the orthogonal depth image) where the maximum in the y-direction is used.

In all these previous cases, no attempt was made to integrate into the image processing algorithm the AUV position data available from the Doppler Velocity Log (DVL) and Inertial Measurement Unit (IMU) systems. In our imaging algorithm, the 2D depth image of a target, i.e. one mapped over x and z or y and z, presents the image strength at the target's z coordinates where the latter is relative to the sediment interface z coordinate directly below the AUV. As a result, the depth coordinate for a target displaced some in-plane distance from the receiver (at x_{lat}, y_{lat} in Fig. 1) will be the sum of the actual burial depth, the depression or elevation of a sloping interface if the interface is not level, and the uncertainty (unknown fluctuations) in the AUV altitude. (See Fig.2.)

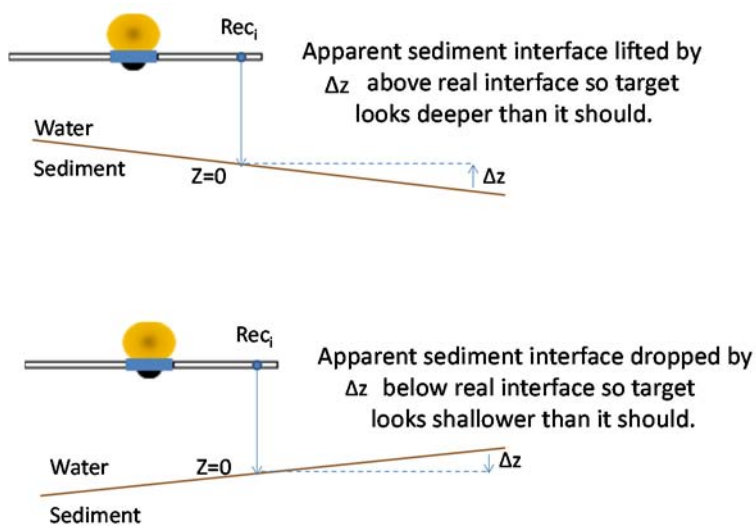

Figure 2. Cartoon illustrating the Δz ambiguity for a sloping sediment when the flight paths are laterally far from the target.

Regarding subtask 2.4, we have generated new images produced after reconfiguring the imaging algorithm to account for AUV position data thus removing the uncertainty due to unknown sensor z coordinates. We considered both AUV altitude and roll but not pitch which we assumed to have a small effect on the receiver height. We can now assume with the actual 3D AUV locations taken into account that the z-locations displayed in the x,z and y,z depth images are accurate (i.e. not an artifact of unaccounted for sensor altitude variations). The remaining ambiguity is now associated with the fact that both the actual target burial depth and AUV altitude are referenced with respect to the sediment interface. In particular, if the sediment interface is sloping in the x or y directions (with reference to Fig. 2), there is a Δz between the sediment interface z co-ordinate directly below the receiver versus one at the x,y target position. As a result, we can only determine the *sum* of the burial depth plus Δz. When the imaged target is not too far laterally from the AUV receivers, we can ignore Δz so that the observed burial depth can be considered the actual target burial depth. For a linearly sloping sediment, a rough rule of thumb is that one could ignore Δz (several centimeters) for lateral receiver-to-target separations less than ~3cm / θ_S where θ_S is the angle in radians between the sloping sediment interface and the horizontal measured in radians. For example, for a 1° sloping sediment (about the maximum seen from the AUV position data), we can ignore Δz if the receiver-to-target lateral separation is less than ~ 2m.

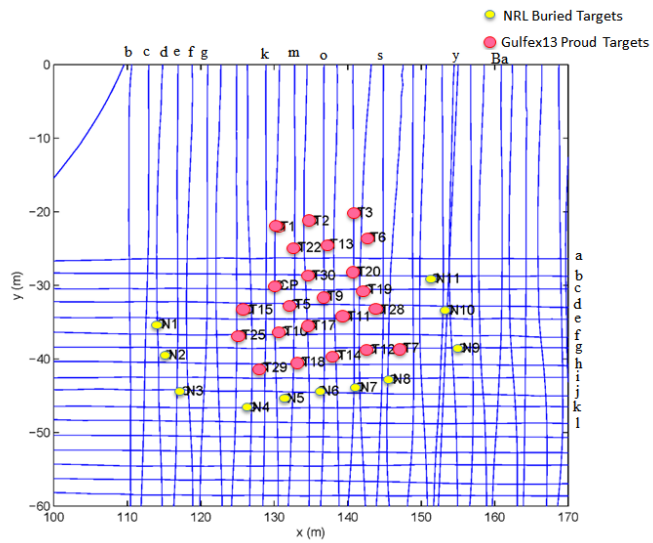

Figure 3. The EW and NS flight paths executed by BOSS over the target field (o NRL buried o TREX13 proud)

First, let us consider the new images obtained from the EW flight paths (see Fig. 3) for the buried NRL targets, N1 –N11. These images are shown in Fig. 4a-4c wherein the three images (plan view and two depth views) are shown for each target. All but two of these images were processed from path h data except for N9 and N11 which used data from paths g and c, respectively. With reference to Fig. 3, for targets N1, N2, and N3 the projected plan view distance between the target and the AUV at its closest approach is ~ 7m, 1.5m, and 5m respectively. (Here and in what follows, the AUV target distance that is given refers to the projected distance in the x,y plane.) The depth images of these targets show them to be below the sediment interface by ~10cm. Next, these distances for N4, N5, N6, N7, N8 are 7.5m, 6m, 4.5m, 4m, and 2.5m, respectively. In these cases, the images show them to be below the sediment surface except for N7 and N8 which appear to be at least partially above the interface. N4 and N5 appear ~10cm below the interface and N6 ~20cm which agrees with our burial plan. Finally, for N9, N10, and N11 these distances are 0m, 10m, and 2.5m respectively. These targets appear to be below the sediment surface except for N10 which appears only partially buried.

We make the following specific comments based on the images about each of these targets.

N1h 60° rocket: Plan view image is ~ the same size as the horizontal target which is probably due to a resolution limit; x,z & y,z images now (correctly) below (10cm) the sediment interface; y,z image has a 60° slant suggesting target burial orientation is along y (although large distance from target i.e. ~8m).

N2h 30° rocket: Plan view image indicates ~30° burial along x axis; x,z & y,z images are now (correctly) below (~10cm) the sediment interface.

N3h horizontal rocket: Ignoring double image, size is 50cm by 30 cm versus 45cm by 13cm; target depth images indicate ~10cm burial as planned; x,z & y,z images also seem to suggest the rocket is not quite horizontally buried.

N4h horizontal 155mm: plan view indicates a 60cm by 30cm size versus 64cm by 16cm. However, depth images indicate near vertical burial and slightly off the x and y directions. N4 is almost 8m away from the h flight path.

N5h 90° rotated horizontal 155mm: these images look similar to those for N4h (as did the old images); target still appears ~ 10cm below the sediment interface as it should.

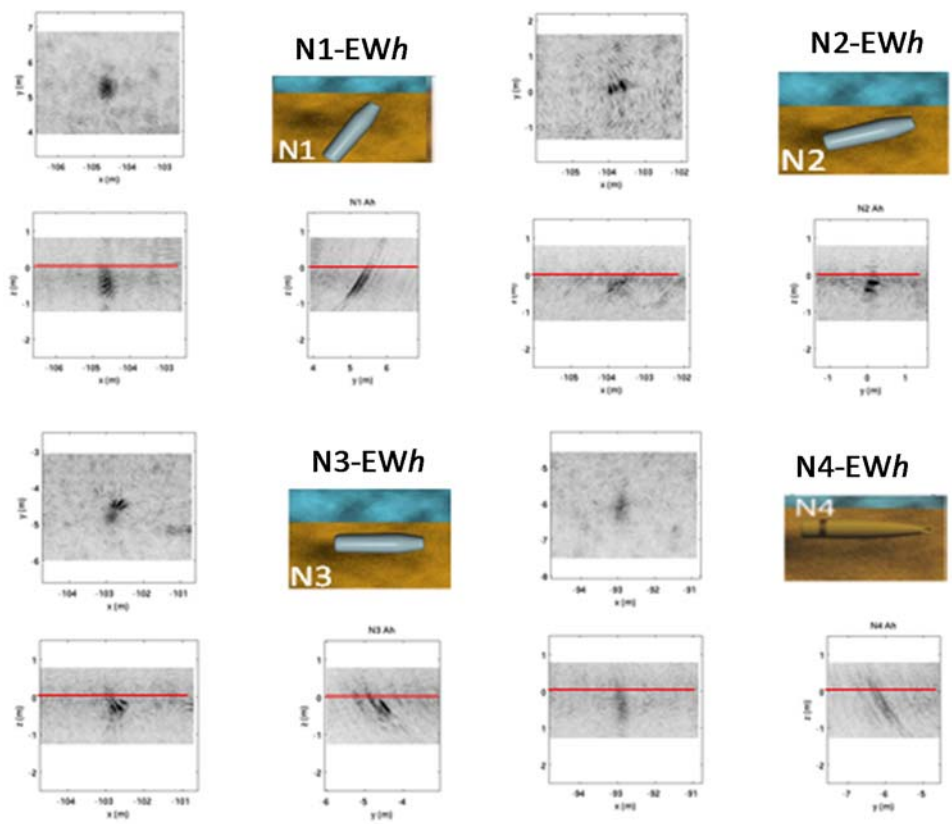

Figure 4a. Plan view and two depth images for N1 through N4 targets using EW flight path *h*.

N6h horizontal deep burial 155mm: Plan view shows a 70cm by 30cm horizontal target. The x,z depth view also correctly shows a horizontal target and one buried ~20cm. However, the y,z image shows a slanted target.

N7h 30° 155mm: x,z & y,z images seem to indicate a partially buried target. Even though N7 is closer to path h, this partial burial may indicate that the sediment is sloping in the y direction here on the right side of the field.

N8h 60° 155mm: x,z image indicates ~50° burial which would be correct; but both x,z & y,z images show some extension above interface although not as much as in the N7 image. Since this target is closer to path h, this may still indicate a sloping sediment.

N9g horizontal 120mm mortar: There is a high background making it hard to interpret all three images. The plan view indicates a horizontal target about 60cm by 40cm; however, this is not at all clear. The z,x and z,y images indicate burial with a large vertical angle. Both of these depth images indicate ~10cm burial as they should since path g is directly over the target.

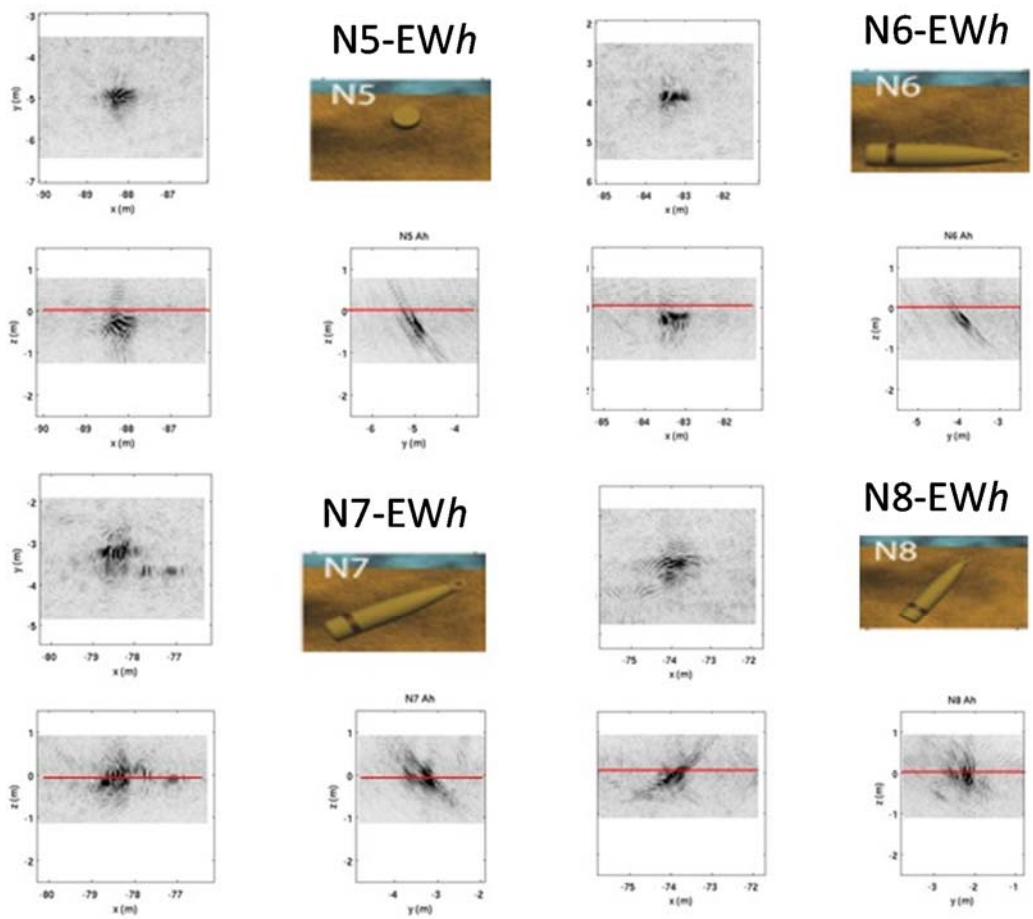

Figure 4b. Plan view and two depth images for N5 through N8 targets using EW flight path *h*.

N10h rock: Unlike the old images, the new depth images indicate a partially buried target as for N7 and N8. However, flight path h is far from the target (~7m) so this may still indicate a sloping interface along y. The x,z and y,z depth images indicate that the plane of the somewhat flat rock is angled near 80° about the x axis, and the x,y plan view image seems to indicate that the somewhat flat rock is buried with its thin axis along the x direction. In point of fact, the three images are very consistent with this, and these images are probably the best to interpret as we discuss later.

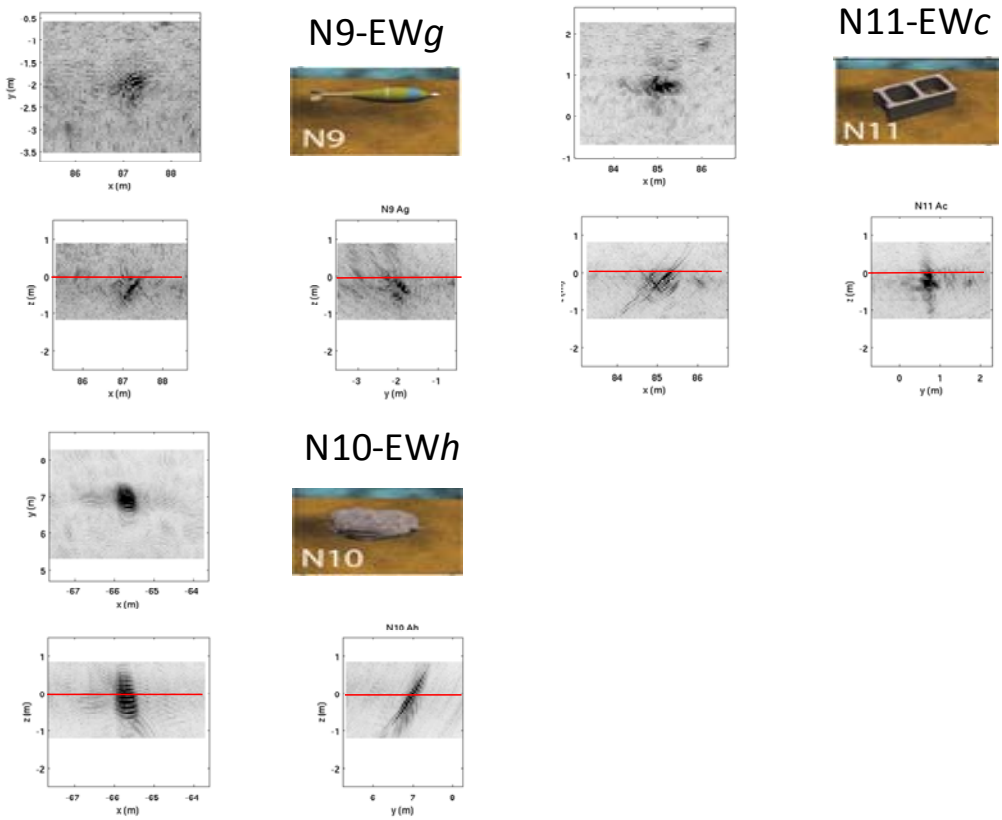

Figure 4c. Plan view and depth images for N9 - N11 targets using EW flight paths *g*,*h*, and *c*, respectively.

N11c cinder block: There are no old images for comparison. In the new images, the depth views indicate a buried target. Taken together, the images suggest that the block is buried horizontally but rolled along its long axis ~80° such that the exposed large holes are mostly in the x,z plane and at a steep angle. The plan view image presents one of the block's solid sides but at an angle (~10°) sufficient to produce a return only from the long edge. The y,z image shows the other solid side rotated ~10° from vertical. This all seems very interpretable as are the rock images.

We now show the images generated from the NS path data in Figs 5a -c.

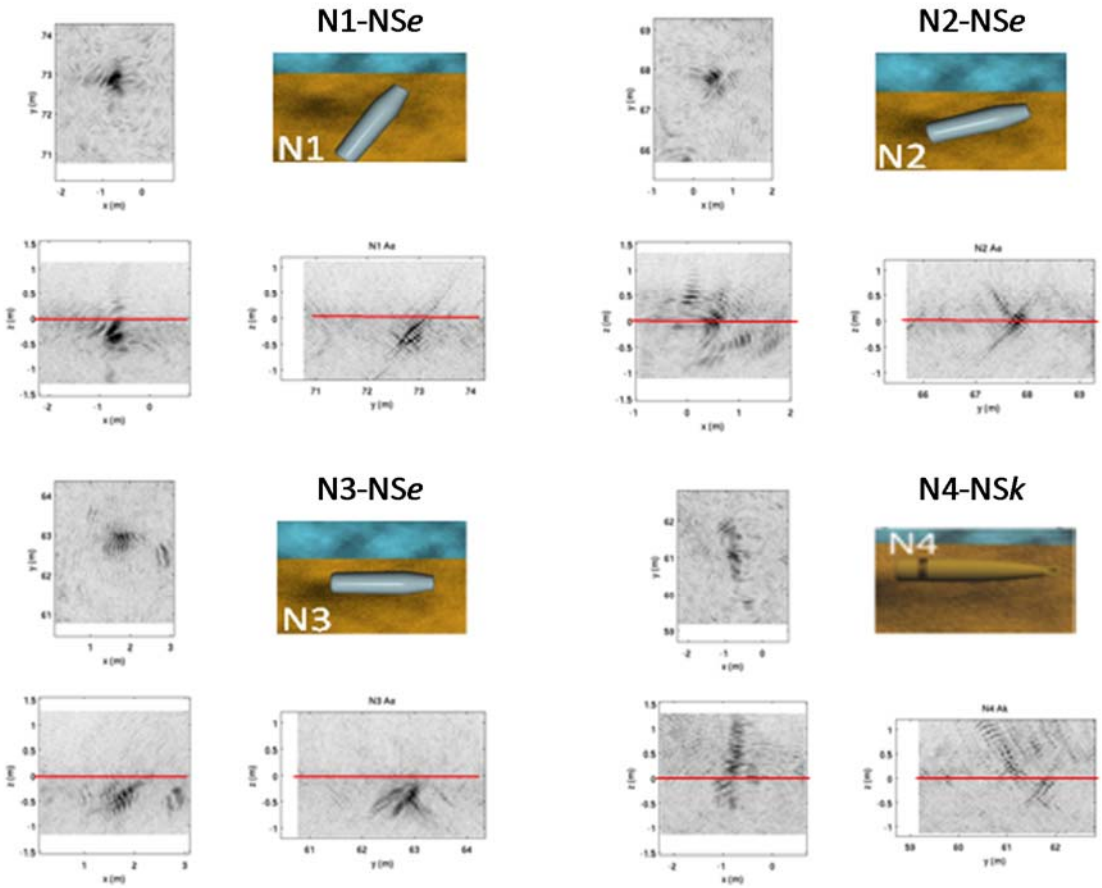

Figure 5a. The plan view and two depth images for N1 through N4 targets using NS flight paths *e* and *k*.

Comparisons of the NS path images with those generated from the EW paths shown earlier seem to indicate that the latter are of higher quality to some degree. This may be due to the fact that in general, the EW flight paths present scattering aspects of the buried targets along their long, cylindrical axes versus circumferentially. Assuming that all the targets are in fact buried as planned, the images processed from the NS flight paths incorrectly show that seven of the eleven are protruding significantly above the sediment surface while only one from the EW paths is incorrect in this regard. Further, the plan view images of the horizontally-buried targets seem to be more reasonable for the EW paths than for the NS paths. In the former case, these plan view images show targets with aspect ratios of about two to one. The actual target aspects are closer to three or four to one. This and the fact that the smallest dimension we see in these images is about 0.25m suggest that our imaging resolution is no better than about three wavelengths at the highest frequency i.e. 20kHz. In contrast, the resolution based on the Airy disc for this highest frequency would give a resolution of about 0.07m at our typical range and for our imaging aperture which resolution is about an acoustic wavelength. We conclude that other factors such as noise, limited navigation information, low scattering levels at certain target aspects, etc. are degrading our images.

Notwithstanding the limited resolution we seem to have achieved, it is interesting to note that the 2-D images for the deepest target burial (20cm for the horizontal 155mm shell i.e. N6) for the EW path *h* (see Fig. 4b) are perhaps the best of the entire set in that the x-z image correctly shows ~ a 20cm burial and the plan view and x,z images are are about the same as they should be.

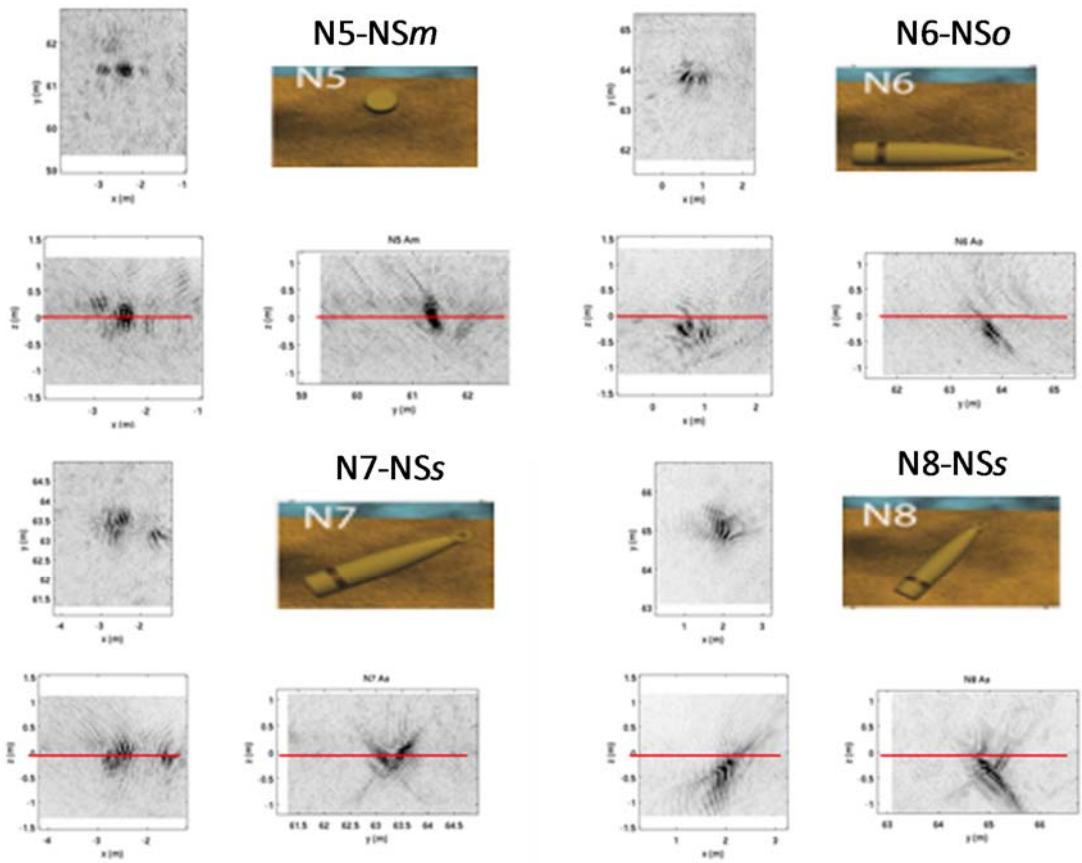

Figure 5b. The plan view and two depth images for N5 through N8 targets using NS flight paths *m, o*, and *s*.

Regarding N10, we will consider the associated images in more detail. We show in Fig. 6 a photo of the rock. Although the actual burial orientation is unknown, we assume a specific orientation and then show that the images are consistent with that assumption. As can be seen from Fig. 4, the flight path (*h*) runs quite a distance from the rock i.e. ~10m. As described in the figure, the rock is assumed buried with its long axis (orange arrow) rotated up out of the horizontal plane ~ 80° about the x axis. For both scans, the height above the sediment interface is 3 meters.

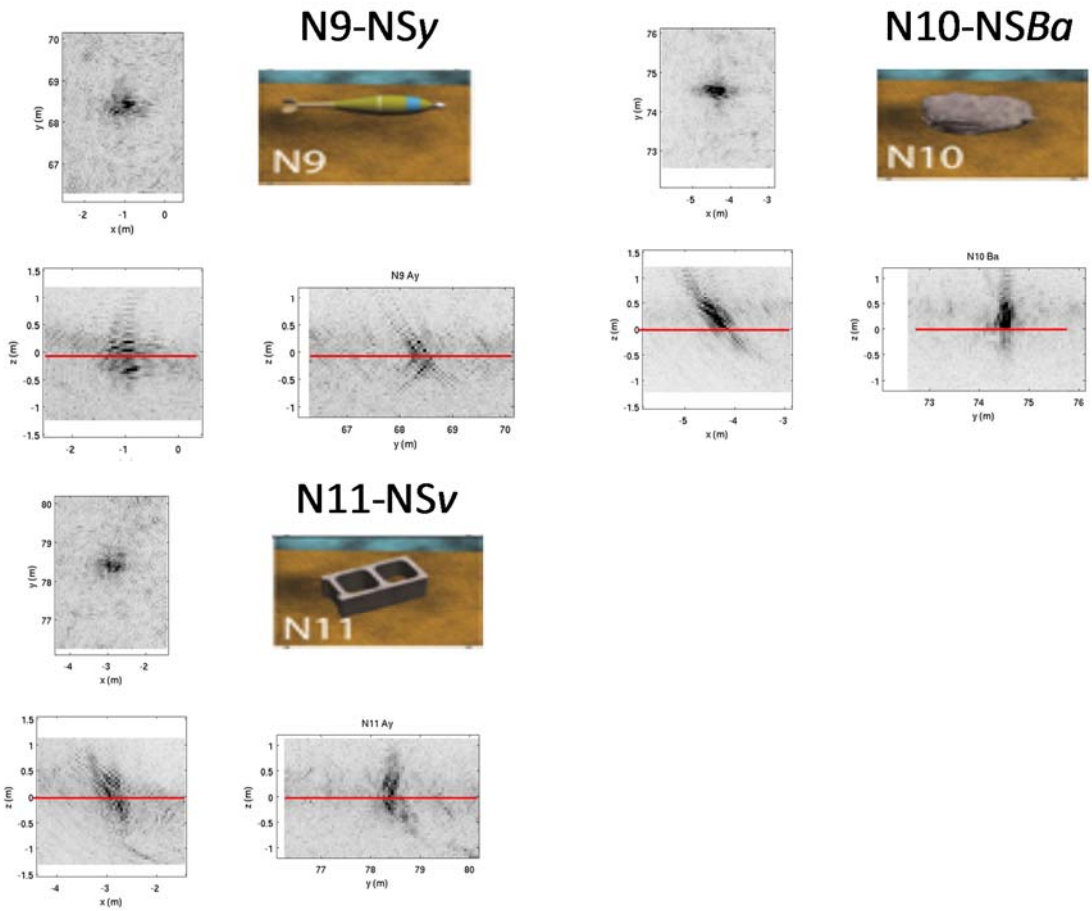

Figure 5c. The plan view and two depth images for N9 through N11 targets using NS flight paths *y*, *Ba*, and *v*.

We show in Fig. 7 the x and y scan images of the buried rock to facilitate understanding the following discussion. Consider first the x scan. The plan view image seems consistent with the rock being buried with its long axis rotated up out of the x,y (horizontal) plane by ~ 80° about the x axis so that what one sees in the plan view image is roughly the top edge of the rock somewhat smeared and oriented along the x axis. Further, with the synthetic scan aperture along the x axis, we might see some spatial structure with x. This is indeed consistent with the plan view image seen in the x scan of Figure 7. This would then imply that one would see a fairly large area in the x,z depth image, and this is indeed the case. Next, considering the detailed shape of the rock (see Fig. 6), in the x scan y,z image one would again see a thin edge of the rock. And since the smaller y coordinates of the rock are deeper, this "thin edge" line would be slanting left to right as indeed it is in the image. Moving to the y scan, the plan view image should present roughly the same as in the x scan but now with some spatial structure in

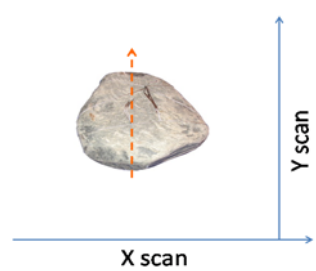

Figure 6. Assumed rock orientation with respect to x, y scans with its long axis (orange arrow) rotated up out of the horizontal plane ~ 80° about the x axis.

y since the synthetic aperture is along y. This is indeed the case, except that the image is not as long along x as it is in the x scan. In the x,z plane, the smaller rock x coordinates are shallower so that the line should slant from right to left as indeed it does. Finally, in the y,z image, the larger rock y coordinates are shallower so that the line would slant upward from left to right. And this is the case as can be seen in Fig. 7. So although the six images of the rock shown in Fig. 7 at first sight seem inconsistent, we have shown that for one plausible rock burial orientation the images are all consistent.

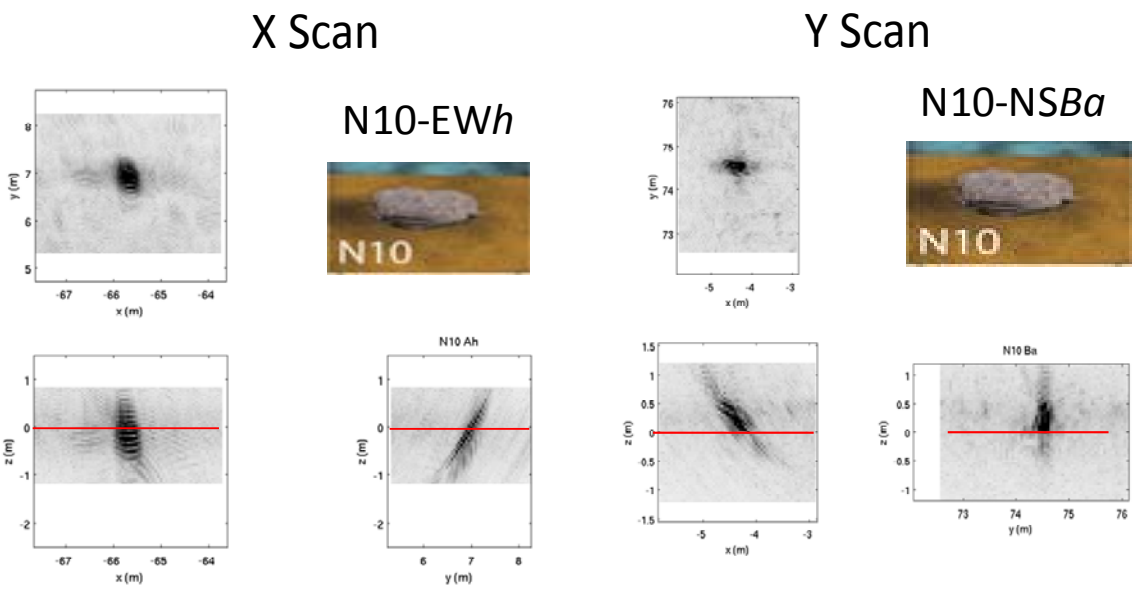

Figure 7. The three 2-D images of the rock (N10) produced from the EW flight path *h* (left) and from the NS flight path *Ba* (right).

In summary, inclusion of the AUV position data in the imaging algorithm has improved both the quality of the images and their ability to correctly register the buried targets with respect to the location of the sediment interface. The few cases in which the images indicate a partially buried target are either correct (the target became somewhat unburied over time) or imply that the sediment surface has a small slope in the *y* direction at the center right of the target field near target N7. The EW path images appear to be better in general than those from the NS paths. This is consistent with the fact that the EW paths sample angles predominately along the cylindrical targets' length versus circumferentially. However, two of the horizontal depth images seem to be at odds with the intended burial angle: N1Hh appears to be oriented along the y versus x axis; and N4Hh appears in the depth images to be vertical rather than horizontal. We do not have an explanation for this. Finally, for the most part the images present targets whose lengths are approximately correct but whose widths are about double what they should be. We take this to be a measure of the resolution limit for our imaging process (data collection, aperture, and imaging algorithm) which would be about 0.25m. At the highest frequency in our band (20 kHz), this is approximately three acoustic wavelengths. From a theoretical point of view, we would expect the following limiting resolutions. Given the 17 kHz bandwidth ΔB, the limiting range resolution ($C/2\Delta B$) would be about 0.04m; and at the center of our band, the limiting cross-range resolution ($\lambda R/(2L_{SAS})$ would be about 0.07m and 0.2m at 2meter and 5 meter ranges, respectively. In the

above, C is the sound velocity, λ the sound wavelength, R the range, and L_{SAS} the synthetic aperture. As in previous BOSS target measurements, the multi-aspect imaging procedures used for BOSS cause image distortion for some target aspects that prevent accurate registration of target dimensions and shape. Further, the conventional SAS method of sweeping the synthetic aperture along track frequently does not allow specular illumination of the UXO targets at aspects that generate echo levels with adequate SNR for imaging. Given these facts, the previously quoted average resolution of 0.25m is not surprising.

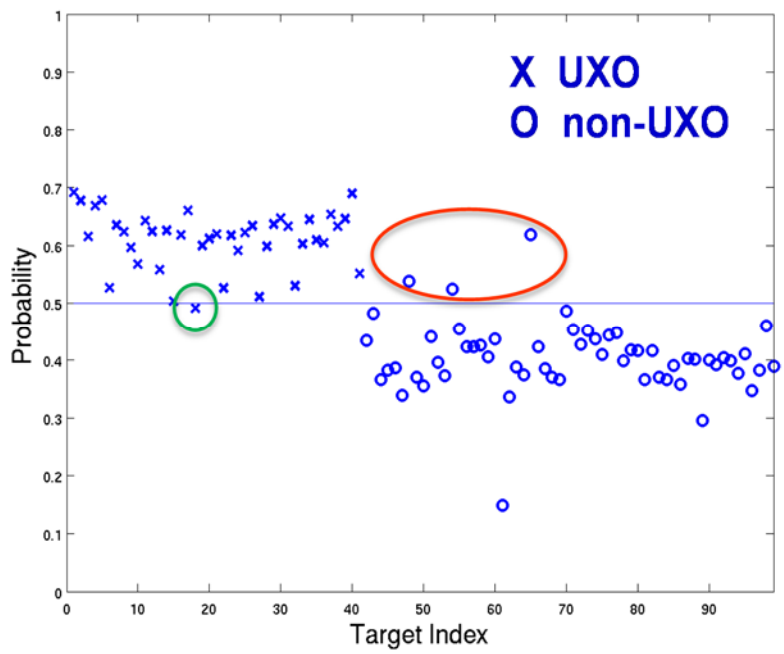

Figure 8a. Discriminatively-trained RVM classification algorithm trained on even numbered source pings and tested on odd numbered pings. Targets include 9 buried UXO and 9 non-UXO – 2 buried and 7 proud. NS paths (3-20 kHz).

SUBTASK 2.5. Include North/South AUV multiple path data in target separation study.

As part of this task, we considered whether the feature separation was better for NS or EW paths. We did not include diagonal paths in this study since the latter were only implemented at 5m altitudes. In the following, we trained *discriminatively*[18] using target data from N1 through N9 (the buried, filled NRL UXO) and false target data from N11 and N12 (the buried cinder block and rock) and proud targets T2, T3, T5, CP, T15, T18, and T19 (the rock, 55 gallon filled

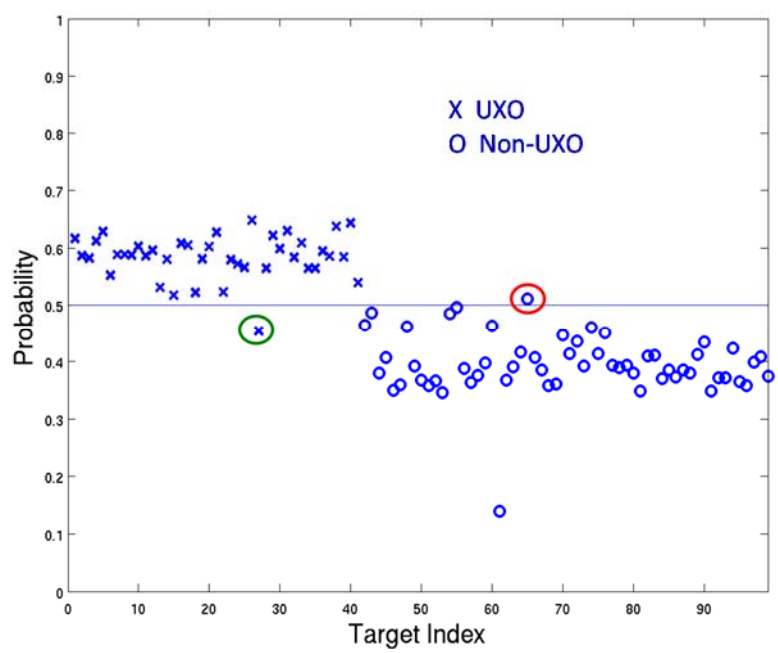

Figure 8b. Discriminatively-trained RVM classification algorithm trained on even numbered source pings and tested on odd numbered pings. Targets include 9 buried UXO and 9 non-UXO – 2 buried and 7 proud. NS paths (3-13.3 kHz).

drum, 5:1 aspect pole section, the panel, 2:1 aspect pole section, cement block, and the tire). The training was done using data from odd numbered source pings and tested on data from even numbered pings versus the original procedure which trained on even numbered receivers and tested on odd. The latter is considered a "sanity check" in the sense that if the chosen features do not separate under these conditions, the features themselves are not useful for target classification.

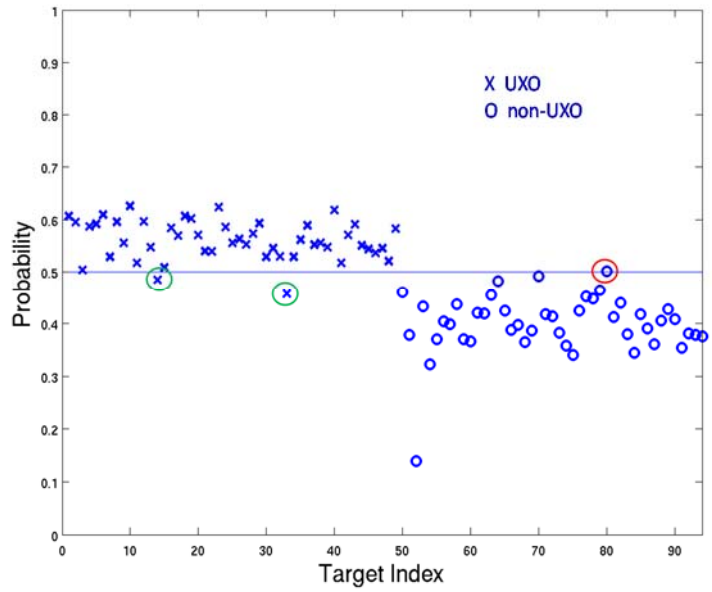

Figure 9. Discriminatively-trained RVM classification algorithm trained on even numbered source pings and tested on odd numbered pings. Targets include 9 buried UXO and 8 non-UXO – 2 buried and 6 proud. EW paths (3 – 13.3 kHz).

The resulting combinatorial probability using the north/south paths is shown in Fig. 8a for the bandwidth 3 – 20 kHz. This is obtained by combining the probabilities over the 40 *y* positions (receivers) i.e. taking the product of the probabilities at each *y* raised to the 1/40 power. Here the target index is sequenced each time a target is seen in a path. (We will see later that the maximum target index for UXO was smaller for NS paths than for EW paths.) The one false negative corresponds to target N5 and path *n* which is the 155mm shell buried horizontally perpendicular to the x direction. Path *n* is about 3m to the right of this target. The three false positives correspond to the following targets: N11 the buried cinder block for path *w* which goes about 1m to its right; T5 the proud 5:1 aspect pole section for path *m* which goes right over the target; and T15 the proud 2:1 aspect pole section for path *m* which also goes nearly directly over the target. Considering that there were on average 5 realizations for each target (five different paths), the four incorrect calls above represent only about 4% of the 96 realizations.

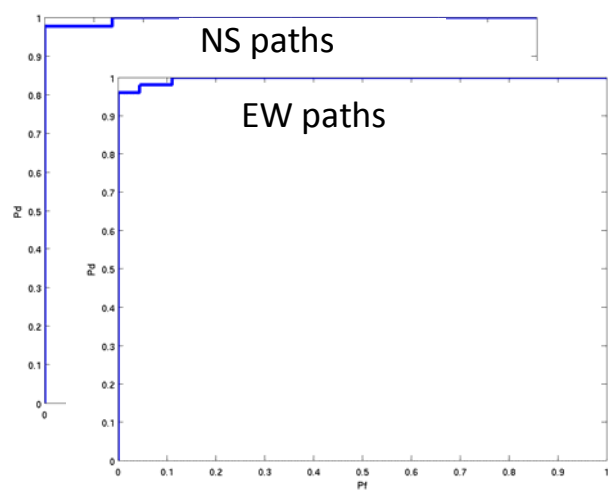

Figure 10. ROC curves associated with the results in Fig 9.

Next, we repeated this identical study but now with the bandwidth consistent with the Nyquist sampling rate, i.e. 3 -13.3 kHz. For this next figure as well as all those following, the bandwidth will be 3 – 13.3 kHz. The new results for the NS paths are shown in Fig 8b. As can be seen, while there is still one false negative, there is only one vice three false positives. We conclude that there is some merit in limiting the bandwidth, although the impact of not doing so is minimal. The one false negative corresponds to target N7 and path n which is the 155mm shell buried nose-up 30 degrees. Path n is about 7m to the right of this target. The false positive corresponds to T15 and path *m* which is the 2:1 aspect pole section. Path *m* goes about 8m to the right of the target.

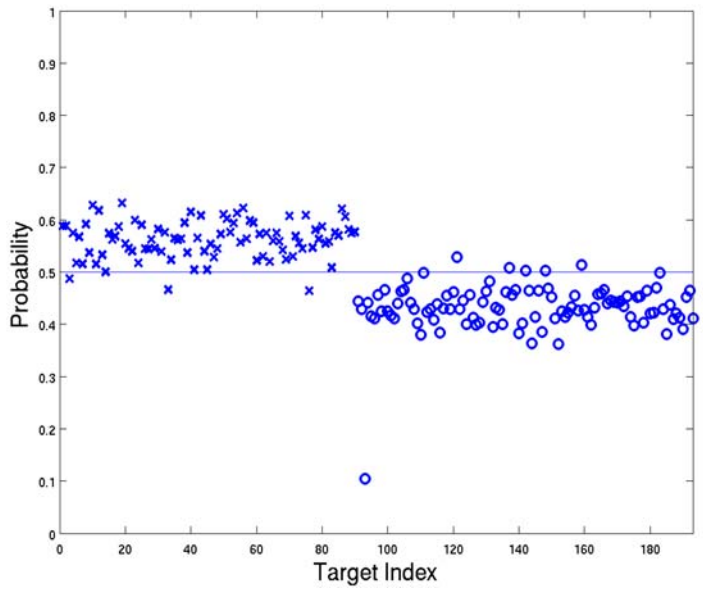

Figure 11. Discriminatively-trained RVM classification algorithm trained on even numbered source pings and tested on odd numbered pings. Targets include 9 buried UXO and 9 non-UXO – 2 buried and 7 proud. NS and EW paths (3-13.3 kHz).

Next we show the results for the east/west paths. In this case, we had no unambiguous image of T3, so we could not include this target. Again we use the combinatorial probability as defined above, and the results are shown in Fig. 9. Overall, the results appear comparable in effectiveness to those shown above for the NS paths. In the horizontal case, the two false negatives are as follows: N4 which is the 155mm shell buried horizontally along the *x* direction and path *h* which is about 7m above the target; and N7 which is the 155mm shell buried nose-up 30 degrees and path *g* which is about 6m above the target. The one false target is T18 which is the proud cement block and path *m* which is 3m above the target.

While the results appear comparable in general to those for the NS paths, there are differences including the following. As can be seen in Fig. 8b, there are many UXO target entries which have probabilities above 0.6 whereas in Fig. 9 there are much fewer. However, the distribution of the false target probabilities is about the same. The ROC curves for each case are shown in Fig. 10. These also indicate a slightly better performance (25% area above the curves) for the NS paths. To the extent that this is meaningful, this improved performance may be related to the fact that for these paths the receivers are moving perpendicular to the cylinder axis for

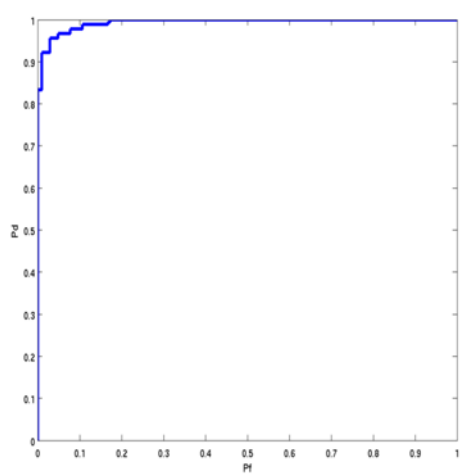

Figure 12. ROC curve associated with the results in Fig 11.

most of the UXO targets. We note that this is opposite to the case for the images where moving along the target's long axis produced better images.

Next we combined the data from the EW and NS paths. These results are shown for the combinatorial probability in Fig. 11. As can be seen, rather than improving the separation, combining the data from the two paths actually resulted in a small degradation in performance. The three false negatives are as follows: N1 which is the five inch rocket buried nose up at sixty degrees and EW path *h* which is about seven meters below the target; N7 which is the 155mm shell buried nose-up thirty degrees and EW path *g* which about seven meters above the target; and N7 and NS path *n* which is about eight meters to the left of the target. The five false positives are as follows: T18 and EW path *i* which is about 2 meters below the target; N10 and NS path *w* which is right on the target; N11 and NS path *w* which is about 1.5 meters to the right of the target; T5 and NS path *m* which is about 0.5 meters to the right of the target; and T15 and NS path *m* which is almost 9 meters to the right of the target. The corresponding ROC curve is shown in Fig. 12 where it can be seen that the separation performance has indeed been degraded.

In summary, we find that the performance of the RVM target feature separation algorithm is slightly better for the NS paths than for the EW paths. For the most part, the NS paths sample the cylinder scattering circumferentially rather than along its length. This is opposite to what we found for the imaging algorithm where images appeared better for the EW paths. In addition, limiting the bandwidth according to the Nyquist sampling criteria improved the performance. Further, using both the NS and EW path data in the training and testing actually degraded the performance. With regard to the percentage of incorrect calls, we found the following: NS paths – 2%; EW paths – 3%; combining paths – 4%. Why this is the case is not currently understood.

SUBTASK 2.6. Include all additional proud targets (+16) in the RVM target separation study

Next, we included all 33 targets both proud and buried. In the list of UXOs, we included the 9 buried, epoxy-filled UXOs (N1 – N9) and the 10 proud UXOs (T8, T9, T11, T12, T20, T22, T25, T28, T29, and T30). In the list of non-UXOs, we included the 2 buried targets (N10 and N11)

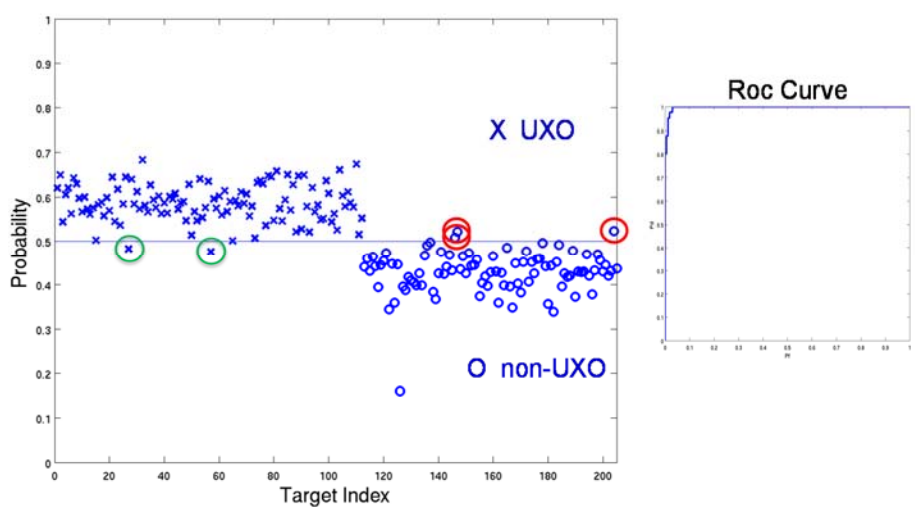

Figure 13. Discriminatively-trained RVM classification algorithm trained/tested on even/odd numbered source pings, respectively. Targets: 9 buried and 10 proud UXO and 14 non-UXO – 2 buried and 12 proud. NS paths (3-13.3 kHz).

and the 12 proud non UXOs (T1, T2, T3, T5, T7, CP, T13, T14, T15, T17, T18, and T19). Again, we trained on even numbered source pings and tested on odd. The results for the combinatorial probability including the ROC curve are shown in Fig. 13. Given the large number of targets and their many realizations (~ 5 paths for each) and the mixture of both proud and buried targets, we consider this separation result to be very encouraging.

The two false negatives are N7 which is the 155mm shell buried nose-up thirty degrees and NS path *n* and T29 which is the small bullet #2 proud on the sediment surface and NS path *n*. The three false positives are T18 which is the cement block proud on the sediment surface and NS path *n*, T19 which is the tire proud on the sediment surface and NS path *n*, and T14 which is the scuba tank with water and a stem and NS path *s*.

In summary, in this study the chosen UXO targets included those that were both buried and proud and those that were epoxy-filled, air-filled, and one that was water-filled. Except for their internal states, they were all UXOs. The false targets included many non-UXO targets that were both proud and buried. The results above demonstrate that the multi-dimensional feature extracted from the acoustic color maps can indeed separate the detections from these two groups. In fact, the five miss-calls represent less than 3% of the total calls. We would expect that separation of these targets into two slightly different groups than the one described above would still offer reasonable target separation.

SUBTASK 2.7. Analyze acoustic color from non-epoxy-filled UXO (proud) compared to epoxy-filled (buried) UXO.

The set of acoustic color maps generated from the EW paths for eight of the 155mm targets were analyzed. The targets included the epoxy-filled buried targets N4 – N8 and the proud targets T8, T9, T28. We assume that the latter three targets are empty, but we have not been able to clarify the details of their internal state at this time. For this study in particular, we inputted the correct range factor in constructing the acoustic color plots in order to have range-corrected target strength numbers for the comparisons. In particular, the target strength formed from the pressure measured at the receiver at r_n from the scattered echo from the target centered at r_c is given by[4]:

$$\text{Target Strength at } \vec{r}_n = 10\log\left|X_n(\omega)\right|^2$$

$$X_n(\omega) = D_n(\omega)\frac{\left|\vec{r}_n - \vec{r}_c\right|}{e^{ik\left|\vec{r}_n - \vec{r}_c\right|}}$$

$$\text{where } D_n\left(\vec{r}_n \middle| \vec{r}_i, \omega\right) = \frac{P_n\left(\vec{r}_n \middle| \vec{r}_i, \omega\right)}{P_i(\omega)}$$

We examined the acoustic color maps visually for the presence of a frequency/x position (aspect angle) feature that we had seen earlier in laboratory measurements in our free-field[4] and sediment pool facilities[5] and which we had subsequently associated with elastic waves in the epoxy filler material. We considered fifty color maps associated with the eight targets. Thirty of these acoustic color maps were deemed "good" in the sense that presence or non-presence of the specific frequency/angle feature seemed definitive. Using these thirty "good" color maps, 90% were

correct calls and only 10% incorrect assuming that the proud targets were indeed empty. Of the twelve flight paths used in this study, paths *h* and *i* had no associated "wrong" calls while path *l* had the most, i.e. five. Regarding the twenty "ambivalent" color maps, not surprisingly the calls with them split almost equally i.e. 45% correct and 55% incorrect. We believe that these results would improve if we were able to de-convolve the correct incident waveform from the scattered signals (see Subtask 2.8).

Next we trained the RVM algorithm *discriminatively*[18] on even numbered source pings and tested on odd numbered pings using the acoustic color maps. On average, we used the epoxy-filled 155mm shell data collected on seven paths and the empty 155mm shell data collected on five paths.

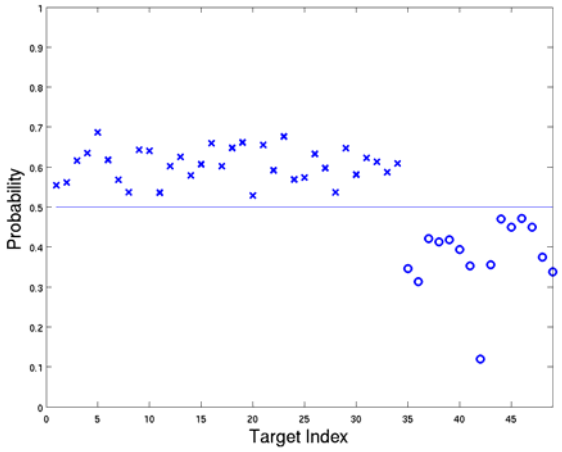

Figure 14a. RVM discriminative algorithm trained and tested on even and odd numbered source pings, respectively using the acoustic color maps. On average, we used epoxy-filled 155mm shell data from 7 EW paths and empty 155mm shell data from 5 EW paths.

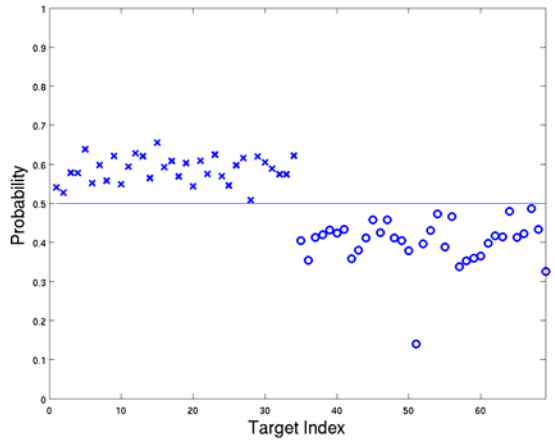

Figure 14b. RVM discriminative algorithm trained and tested on even and odd numbered source pings, respectively using the acoustic color maps. On average, we used epoxy-filled 155mm shell data from 7 EW paths and empty 155mm shell data collected on 7 EW paths.

The results for the combinatorial probability of being an epoxy-filled 155mm shell is shown in Fig. 14a. As can be seen, there is perfect separation between the two target sets. After we had carried out this target separation study, we learned that the two targets called "bullet #1" (T25) and "bullet #2" (T29) are also 155mm shells. Further, T25 is air filled while T29 is water filled. We added the data from these two targets to the false target data and retrained and retested. The results are shown in Fig. 14b. As can be seen, the epoxy-filled 155mm shells still separate from the empty and water-filled shells.

In summary, the fact that the multi-dimensional feature extracted from the acoustic color maps can be used to separate the epoxy-filled shells from the others is very encouraging. However, we point out that these two target sets differ not only because of the presence of epoxy filler material or the lack thereof, but also by the fact that one target set is buried while the other is proud. In this regard, future measurements ought to include epoxy-filled and empty UXO that are all buried.

SUBTASK 2.8. Perform acoustic BOSS source calibration in the NRL near-field holography facility.

The necessary facility preparations were made for executing the source calibration measurements for BOSS in the NRL Laboratory for Structural Acoustics. We took delivery of BOSS June 9, 2014 and successfully mounted the AUV-based system in our Building 5 structural acoustic pool facility (see Fig. 15) without any problems. Measurements began on June 12, 2014. Given the time allotted for BOSS at NRL (two weeks), we did not attempt a full holographic scan of the source/vehicle system. Rather, we designed a more limited data collection plan which gave us radiated pressure (phase and amplitude) at 3.5 meter distances over five complete rings in steps of one/half degree. For four of the rings, the vehicle was hung vertically in a manner permitting 360 degree vehicle rotation in steps of 1/2 degree. As shown on the left of Fig. 16, the monitoring hydrophone was positioned 3.4 meters from the vehicle at four different vertical locations (near the nose, adjacent to the projector, near the wings, and near the tail section). Data was collected at each of these positions over the full 360 degrees. A final fifth ring configuration was executed in which the vehicle was hung horizontally and the receiver rotated 360 degrees in the horizontal plane. (See the right side of Fig. 16.) Measurements ended on June 18, 2014, and BOSS was shipped back to Panama City, FL on June 23, 2014. We show in Fig. 17 the frequency-angle plots for the response measured on each of the five hydrophones in Fig. 17. We also show in Fig. 17 (bottom right) the response that would be seen if the source were indeed a monopole (omnidirectional) and it were excited by the chirp electrical waveform used in our experiments. To obtain this response map, we used the TVR curve provided by the source manufacturer for the actual BOSS source, a ITC-1007 omnidirectional 6 inch diameter zirconate titanate transducer.

Figure 15. The NRL Structural Acoustic Pool facility.

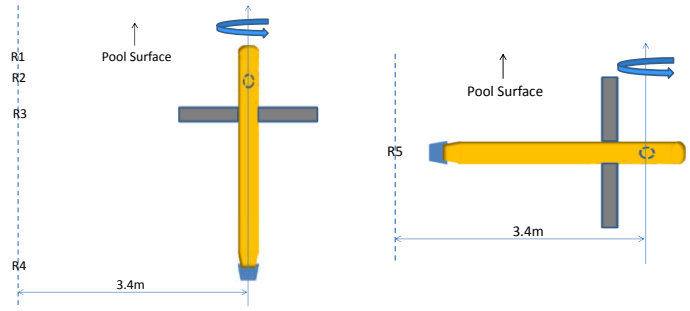

Figure 16. The two orientations for hanging BOSS in the NRL Structural Acoustic Pool facility.

Clearly, the coupled source/AUV system does not radiate as a mono-pole. Unlike the isolated spherically radiating source, at any particular frequency, the acoustic pressure fluctuates considerably with direction. As far as we know, most post mission processing analyses (PMA) of BOSS data to date assume an incident signal independent of angle, and it is reasonable to assume that this assumption impacts the various constructs obtained from the BOSS data collection flights. This would include imaging as well as acoustic color, although what one does with each of these constructs in terms of target classification will determine the ultimate impact.

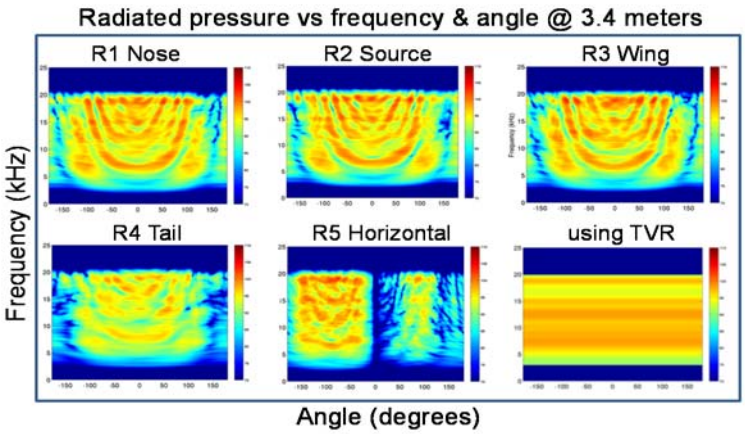

Figure 17. Source pressure levels in dB measured at the 5 receivers 3.4 meters from BOSS as it is rotated in steps of 0.5 degrees. Lower right: what the pattern would be were the BOSS source omnidirectional.

characteristics at the scattering target. One approach involves the development of a structural acoustic model describing the angle-frequency characteristics that is validated by the five ring data we have collected. This model would then be used together with holographic projection methods to obtain a close approximation to the actual source characteristics on the sediment. This model would then be integrated into the algorithms we use to obtain the various constructs from the BOSS receiver data.

Subtask 2.9 Using new BOSS source calibration data, generate and analyze specular-filtered plan view images of the buried UXO.

The data obtained from the BOSS calibration measurements (Subtask 2.8) has been processed and analyzed. The measurements had been made in the NRL Building 5 structural acoustic pool facility and involved the following five configurations. The vehicle was hung vertically in a manner permitting 360 degree vehicle rotation in steps of 1 degree. The monitoring hydrophone was positioned 3.4 meters from the vehicle at four different vertical locations (near the nose, adjacent to the projector, near the wings, and near the tail section). Data was collected at each of these positions over the full 360 degrees (the circumferential data). A final fifth configuration was executed in which the vehicle was hung horizontally and the receiver rotated 360 degrees in the horizontal plane. The first four rings of data

We show in Figs 18 and 19 the time waveforms and frequency response of each of the four rings at 0 degrees. For comparison, we show the same signal and spectrum assuming the source is omnidirectional and excited by our particular chirped waveform in the lower left hand side in each figure.

Currently, we are considering how one might use the above limited BOSS calibration data in order to intuit more accurate incident sound spatial and temporal

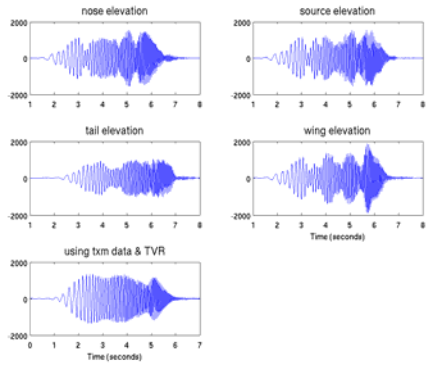

Figure 18. The measured time waveforms at the R1 through R4 receivers and the prediction from TVR curve.

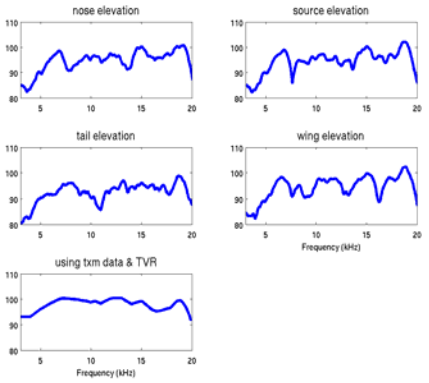

Figure 19. The measured signal spectra measured at the R1 through R4 receivers and the prediction from TVR curve.

viz. the circumferential data spaced along the AUV length clearly show time waveform variations from what is expected from the isolated source confirming our earlier suspicion. Further, there is strong azimuthal pseudo-periodic structure in the source radiation pattern demonstrating that the source as mounted on the AUV is far from an omni-directional radiator. This means that assuming an incident pressure waveform on the sediment interface below that is (1) a simple convolution of the electrical waveform with the isolated source transfer function and (2) spatially uniform is not justified. As far as we know, these assumptions have been made by all previous BOSS users including ourselves up to now. This complication impacts all the post measurement analysis (PMA) results, particularly those involving large angular apertures and/or range variations in the data collection. This task focused on image improvement was originally planned recognizing the problems associated with problem (1) above but not problem (2). Redoing the images in a meaningful manner will now first require the resolution of both issues (1) and (2). Addressing the latter issue will require a significant study to develop at least an approximate approach for obtaining the more complicated spatially dependent pressure waveforms incident on the sediment interface as a function of range and angle. We devoted the remaining resources allocated to Subtask 2.9 to making progress on this issue. Our approach involves development of an understanding of the structural acoustics of the coupled source/AUV radiation problem and the subsequent development of an associated model which will allow projection of our ring-measured data to the 3-D space below. Currently, we are considering how one might use the above limited BOSS calibration data in order to intuit more accurate incident sound spatial and temporal characteristics at the scattering target. One approach involves the development of a structural acoustic model describing the angle-frequency characteristics that is validated by the five ring data we have collected. This model would then be used together with holographic projection methods to obtain a close approximation to the actual source characteristics on the sediment. This model would then be integrated into the algorithms we use to obtain the various constructs from the BOSS receiver data.

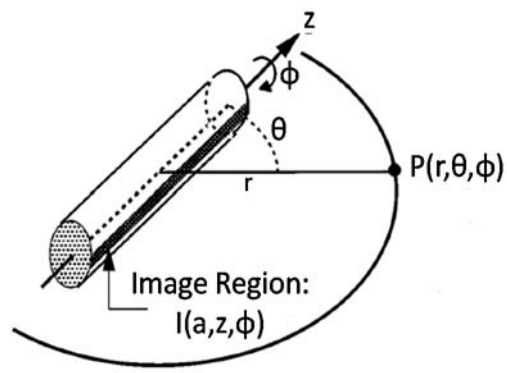

Figure 20. Geometry describing the mapping between the measured source radiation pattern and the radiating source strength spatial distribution.

To this end, we have just completed the generation of supersonic intensity images[19] to identify the actual radiating source spatial distribution as it exists over the surface of BOSS for the acoustically coupled source/vehicle over the length of the AUV. With reference to Fig. 20, the supersonic imaging algorithm constructs the radiating source strength distribution as a function of z, φ, and frequency given the measured source radiation pattern given in Fig. 17 of Subtask 2.8 and marked R5 Horizontal.

The resulting supersonic images are shown in Fig. 21 for the two halves of the cylindrical surface, one labeled bottom side (the half containing the source) and the other labeled top side (the half

area opposite the source). Immediately we see two characteristics: (1) the radiation is coming from the 25% or less of the surface that includes the source; and (2) the bottom side source distribution is two to three times wider than that for the top side.

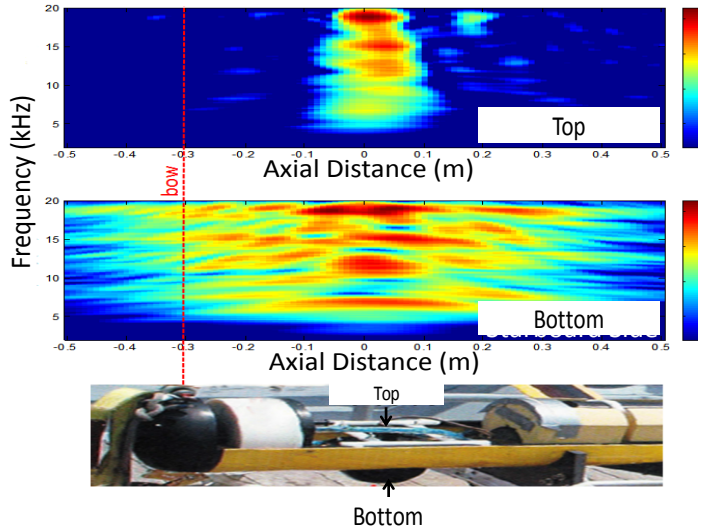

Figure 21. The supersonic images mapped onto the BOSS AUV upper half and the BOSS AUV lower half. The photo indicates the actual locations on BOSS.

Examination of the data shown in Fig 17 of the Subtask 2.8 section for the four circumferential rings indicates that the basic frequency/angle structure is about the same for all four rings. Further, the frequency structure shows the frequency modulation for zero angle has a periodicity Δf of about 3 kHz. If this were associated with the resonances of a rectangular cavity, one would estimate the width of the cavity to be $T = C/(2\Delta f)$ or about 10 inches if the cavity were water filled. Here C is the speed of sound. This is close to the diameter of the BOSS AUV which is 12 inches.

These three findings – (1) the supersonic image localized to the cavity containing the source; (2) the frequency/angle structure being the same along the length of the AUV; and (3) the periodicity in frequency at zero angle being consistent with resonances of a cavity about the dimension of the AUV diameter - lead us to conclude that the important structural acoustic interaction to consider is that between the spherical source, its mounting structure, and the associated short cylindrical section of the AUV. The next step is to develop a relatively simple model to predict our measured results and then to integrate this into our PMA of current and future BOSS data.

CONCLUSIONS TO DATE

The following conclusions are based on the results reported both here and in the MR2103 Final Report dated April 2014.

(1) Image formation of buried targets using SAS-processed scattering data and AUV positional data collected using BOSS executing linear tracks over the buried targets can be used to garner approximate dimensions, burial orientation, and burial depth of typical UXO targets. With the AUV track length on the order of 10m, rough spatial resolutions of 0.25m in both the along-track and cross-track directions were achieved. From a theoretical point of view, we would expect the following limiting resolutions. Given the 17kHz bandwidth, the limiting range resolution would be about 0.04m ($C/2\Delta B$); and at the center of our band, the limiting cross-range resolution would be about 0.075m and 0.15m at 2meter and 5 meter ranges, respectively ($\lambda R/(2L_{SAS})$. In BOSS target measurements, the multi-aspect imaging procedures used in BOSS post-processing cause

image distortion for some target aspects that prevent accurate registration of target dimensions and shape. Further, the conventional SAS method of sweeping the synthetic aperture along track frequently does not allow specular illumination of the UXO targets at aspects that generate echo levels with adequate SNR for imaging. Imaging with data from tracks along the length of the cylindrical targets appears somewhat better than from tracks along the circumference. It remains to be seen whether combining orthogonal path data in the imaging process improves the images.

(2) The high-dimensioned feature extracted from acoustic color (target strength versus aspect or position and frequency) has been shown to separate the buried UXO from the buried and proud non-UXO using an RVM classification algorithm. Further, this same RVM-processed multi-dimensional feature separated the epoxy-filled 155mm shells from the empty ones. For these targets, visual test in the acoustic color maps for the presence of the elastic wave feature at quartering aspects also statistically separated the empty and filled shells.

While this is encouraging, the following issues remain to be addressed. First and foremost, practical approaches for training the RVM algorithm remain to be developed. Second, there is much to be gained by optimizing the acoustic color features used in the algorithm. Connected with this is development of how to combine data from various sonar tracks including those orthogonal to one another. Progress here would increase the feature separation between UXO and false targets greatly improving the robustness of the RVM classification algorithm.

(3) Detailed BOSS projector/AUV radiation measurements over frequency and angle made in the NRL structural acoustic facility clearly demonstrate that the assumption made in this and all previous BOSS PMA exercises i.e. that the projected sound is spherically symmetric is grossly incorrect. The associated inadequate knowledge of the frequency/angle source characteristics (i.e. the incident pressure waveform amplitude and phase) over the interrogated sediment surface clearly has an impact on the quality of both the images (especially what is called the specular-filtered, elastic highlight image) and the acoustic color constructs as well. What is required now is a method to incorporate these calibration source characteristics into both the imaging and acoustic color PMA procedures. We would expect that success here would lead to significant improvements in the images but especially to the target classification results.

LITERATURE CITED

1. B. H. Houston, J.A. Bucaro, T. Yoder, L. Kraus, and J. Tressler, J. Fernandez, T. Montgomery, T. Howarth, “Broadband Low Frequency Sonar for Non–Imaging Based Identification,” IEEE Oceans 2002.

2. J. A. Bucaro, B.H. Houston, M. Saniga, H. Nelson, T. Yoder and L. Kraus, and L. Carin, “Wide Area Detection and Identification of Underwater UXO Using Structural Acoustic Sensors,” 1st Annual SERDP Report, NRL/MR/7130—07-9014, January 12, 2007.

3. J.A. Bucaro, B.H. Houston, M. Saniga, A. Sarkissian, H. Nelson, T. Yoder, L. Kraus, and L. Carin, "Wide Area Detection and Identification of Underwater UXO Using Structural Acoustic Sensors – 2nd Annual SERDP Report," NRL/MR/7130—08-9103, August 12, 2008.

4. J.A. Bucaro, B.H. Houston, M. Saniga, L.R. Dragonette, T. Yoder, S. Dey, L. Kraus, and L. Carin, "Broadband Acoustic Scattering Measurements of Underwater Unexploded Ordnance (UXO)," J. Acous. Soc. Am. 123, 738-746 (2008).

5. J. A. Bucaro, H. Simpson, L. Kraus, L. R. Dragonette, T. Yoder and B. H. Houston, "Bistatic scattering from submerged unexploded ordnance lying on a sediment," The Journal of the Acoustical Society of America 126 (5), 2315-2323 (2009).

6. J. A. Bucaro, B.H. Houston, H. Simpson, L. Kraus, T. Yoder, M. Saniga, A. Sarkissian, and L. Carin, "Wide Area Detection and Identification of Underwater UXO Using Structural Acoustic Sensors," 3rd Annual SERDP Report, January 2009.

7. J. A. Bucaro, B.H. Houston, H. Simpson , M. Saniga, A. Sarkissian, D. Calvo, L. Kraus, T. Yoder and L. Carin, "Wide Area Detection and Identification of Underwater UXO Using Structural Acoustic Sensors," 4th Annual SERDP Report, July 21, 2010.

8. J. A. Bucaro, B.H. Houston, H. Simpson, Z. Waters, M. Saniga, S. Dey, A. Sarkissian, D. Calvo, L. Kraus, and T. Yoder, "Wide Area Detection and Identification of Underwater UXO Using Structural Acoustic Sensors," Final Report SERDP Report, July 8, 2011.

9. S. G. Schock and J. Wulf, "Buried Object Scanning Sonar for AUV's," Oceans 2003, 494-499.

10. J.A. Bucaro, A. Sarkissian, B.H. Houston, H. Simpson, Z.J. Waters, D. Amon, K. Jig, S. Liskey, and T. Yoder, "Structural Acoustic UXO Detection and Identification in Marine Environments – Final Report to SERDP MR-2103 (2014).

11. M. Tipping, "Sparse Bayesian Learning and the Relevance Vector Machine," Journal of Machine Learning Research/, vol. 1, pp. 211-244, 2001.

12. Z. J. Waters, H.J. Simpson, A. Sarkissian, S. Dey, B.H. Houston, J.A. Bucaro, and T. Yoder, "Bistatic, Above-critical Angle Scattering Measurements of Fully Buried Unexploded Ordnance (UXO) and Clutter," J. Acous. Soc. Am., vol. 132, pp. 3076–3085 (2012).

13. S. Dey and D.K. Datta, "A Parallel hp-FEM Infrastructure for Three Dimensional Structural Acoustics," Int. J. Numer. Methods Eng. 68, 583-603 (2006).

14. Saikat Dey, Angie Sarkissian, Eris S. Mestreau, Brian H. Houston, and Larry Kraus, "Three-Dimensional Structural-acoustics Modeling and its Validation for Free-field and Littoral Environments," J. Acoust. Soc. Am. 125, 2702 (2009).

15. Joseph A. Bucaro, Zachary J. Waters, Brian H. Houston, Harry J. Simpson, Angie Sarkissian, Saikat Dey, and Timothy J. Yoder, "Acoustic identification of buried underwater unexploded ordnance using a numerically trained classifier," J. Acoust Soc Am 132, 3614-1617 (2012).

16. Paul J. Carroll, "Underwater (UW) Unexploded Ordnance (UXO) Multi-Sensor Data Base (MSDB) Collection," Final report SERDP Project MM-1507, July 2009.

17. Robert A. Leasko, Charles L. Bernstein, Richard Holtzapple, and Jesse I. Angle, "Munitions Detection using Unmanned Underwater Vehicles Equipped with Advanced Sensors," Interim Report, ESTCP Project MR-201103, June 29, 2012.

18. I. Ulusoy and C. M. Bishop, "Generative versus discriminative methods for object recognition," in Computer Vision and Pattern Recognition, 297 IEEE Computer Society conference (2005), Vol. 2, pp. 258–265.

19. E. G. Williams, Fourier acoustics: Sound radiation and nearfield acoustic holography. (Academic Press, San Diego, 1999).

APPENDIX

The wing BOSS system (photograph shown in Fig. A1) is designed to scan for buried underwater objects using two 1m hydrophone arrays mounted as wings of an autonomous underwater vehicle (AUV). An under-view and head-on view of the system is shown in the diagram in Fig. A2. The

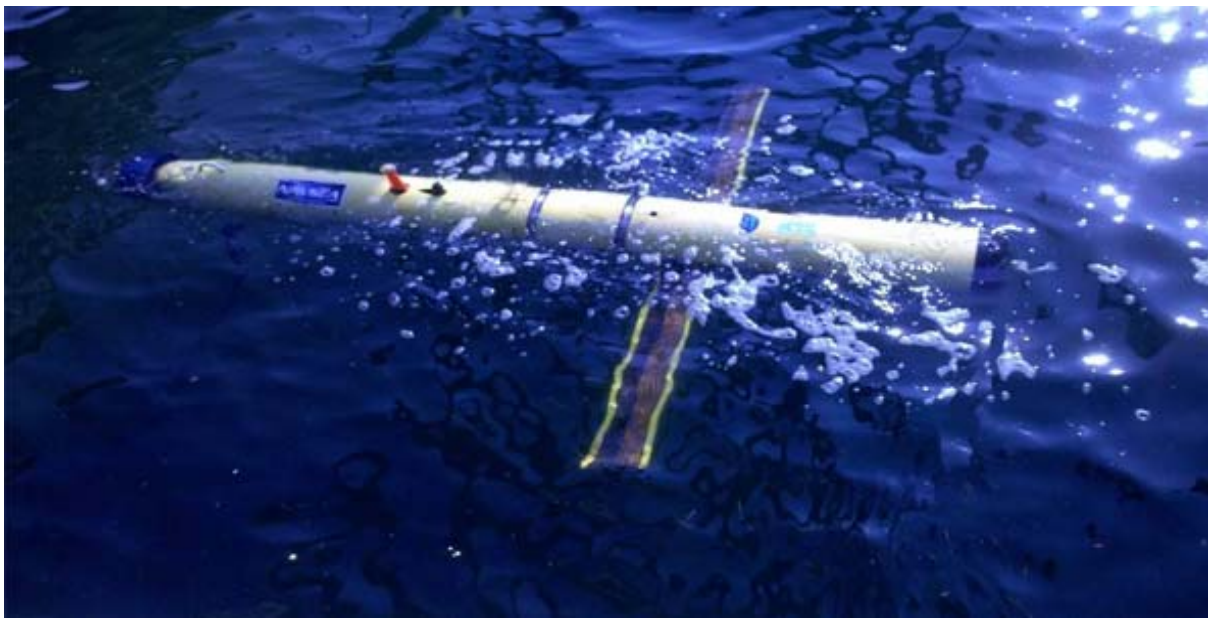

Figure A1. Photograph of BOSS in the Water.

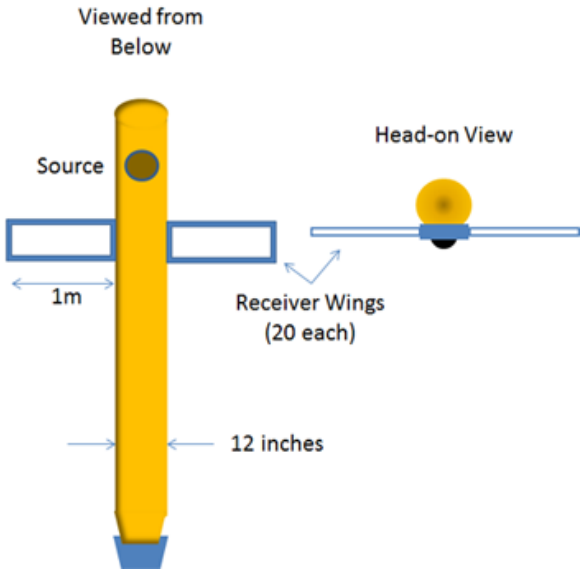

Figure A2. Plan view and head-on view of BOSS.

AUV system used here is the Reliant Bluefin 12 vehicle designed and fabricated by Bluefin Robotics. (See Figure A3.) Each wing contains 20 hydrophone channels, yielding a 40-channel strip array used to collect the sonar returns. This system uses an omnidirectional projector that transmits a FM pulse over the frequency band 3-20 kHz. The wing BOSS is smaller and more mobile than the previous BOSS vehicles, as the wing arrays tend to produce less drag than the large circular array.

In order to improve the resolution of target imagery, the wing BOSS utilizes time-delay focusing extended to hydrophone data collected over several transmissions. With synthetic aperture processing, the along-track resolution of target imagery improves with distance traveled while forming the synthetic

aperture. The use of synthetic aperture processing also allows the along-vehicle dimension of the array to be significantly reduced compared to a real array thereby reducing the hydrophone array drag and surface area and increasing the ease with which BOSS can be deployed on an AUV.

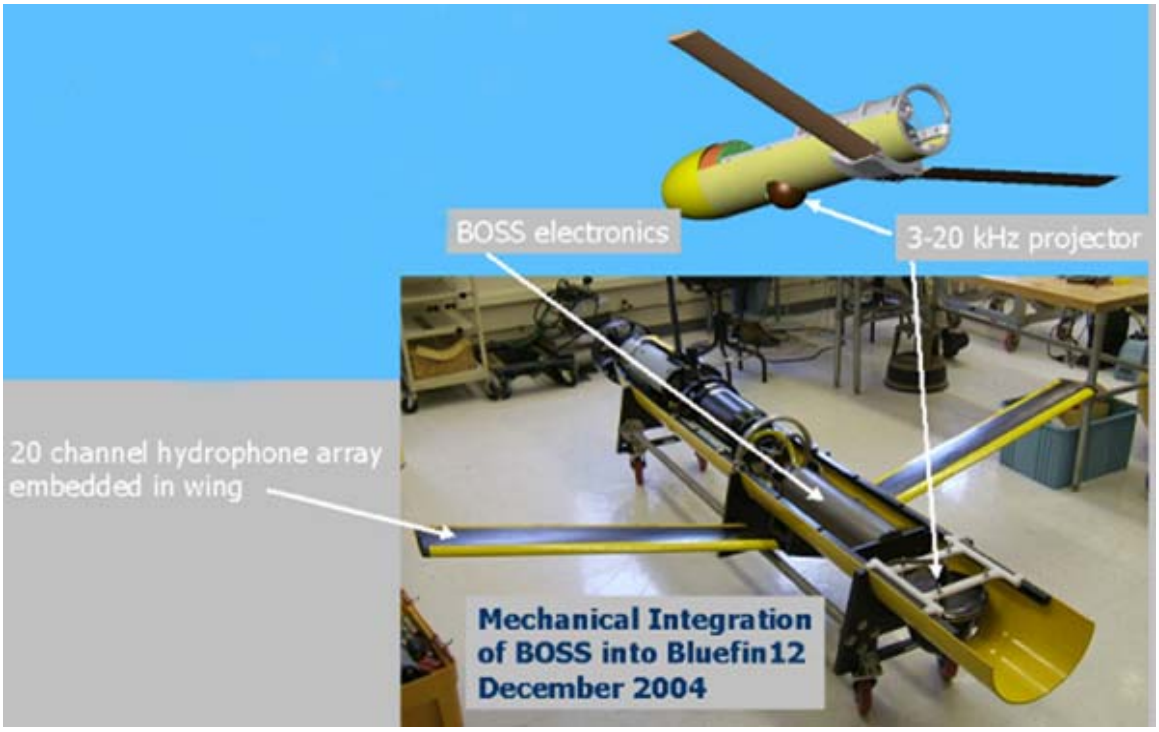

Figure A3. Photograph of BOSS prior to complete assembly showing some of the internal components.

Three-dimensional SAS imagery is generated using a navigation solution based on measurements from a Doppler Velocity Log (DVL) and an Inertial Measurement Unit (IMU) to time-delay and coherently sum matched-filtered phase histories from subsurface focal points over a large number of pings. The focused data consist of a large set of three dimensional SAS data cubes created by a sliding window of ping intervals, where adjacent data cubes have greater than 90% overlap. By using navigation/registration information, these data cubes are fused into a single large three dimensional dataset, in which each voxel's intensity is the maximum intensity of the co-registered voxels across all original data cubes. For improved image contrast, the intensity of the specular seafloor return (a shallow swath of voxels beneath the platform) is spatially nullified with an automated process employing measured backscatter statistics. Fig. A4 shows mosaics of top-view maximum intensity projections for data runs collected over the TREX13 target field in the Gulf of Mexico. These results were obtained by R. Holtzapple and N. Pineda as reported in their "Quick Look Analysis" document following the June 2013 BOSS exercises.

As can be seen in the top portion of Fig. A4, all proud and buried targets in the field of view of these 3 meter altitude west-east flights are detected via the plan view images displayed in this figure. The three 2-D images generated from these are shown for four of the buried NRL targets in the lower part of the figure. In each of these, the plan view image is repeated in the upper left while the images with depth (x,z and y,z) are shown in the lower left and upper right images,

respectively. As can be seen, the N5 and N6 (*x*,*z*) images correctly show horizontally buried targets while those for N7 and N8 correctly show targets buried nose up at about 30° and 60° angles.

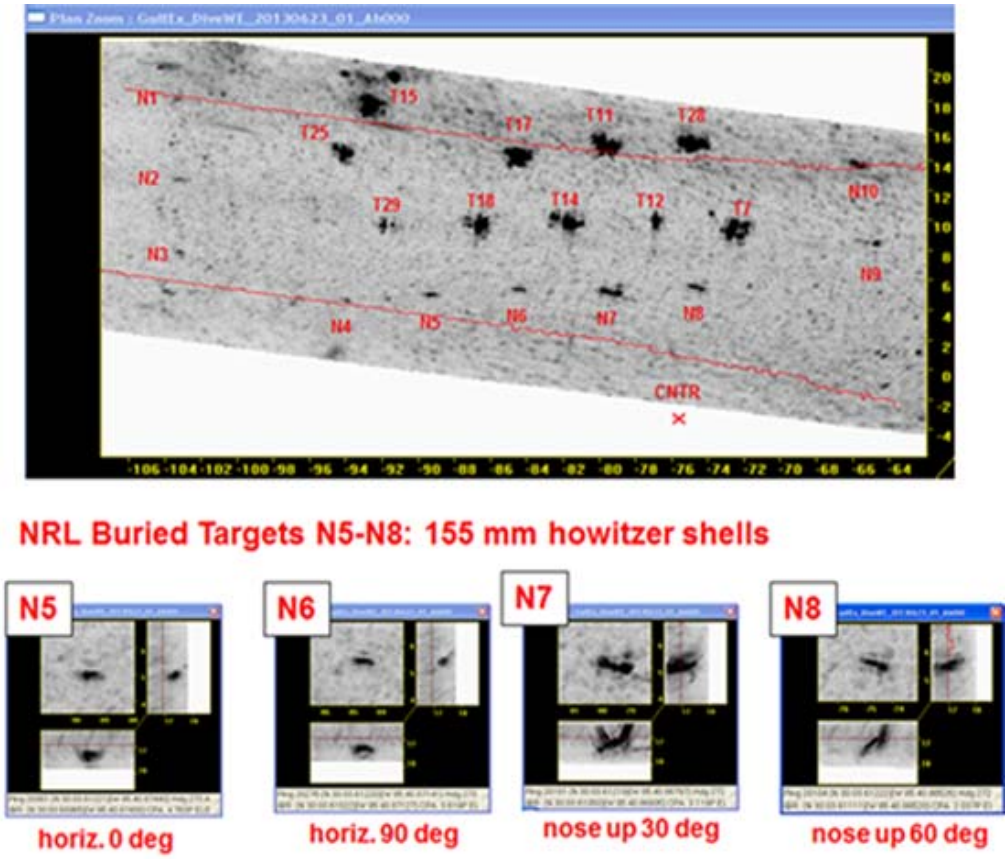

Figure A4. Preliminary 3-D images obtained from June 23, 2014 BOSS data by Richard Holtzapple and Nick Pineda.